

**NASA**  
**Technical**  
**Paper**  
**3361**

October 1993

1N-32  
193039  
49P

# Analysis of Electromagnetic Scattering From Irregularly Shaped, Thin, Metallic Flat Plates

Manohar D. Deshpande,  
C. R. Cockrell,  
Fred B. Beck,  
Erik Vedeler,  
and Melissa B. Koch

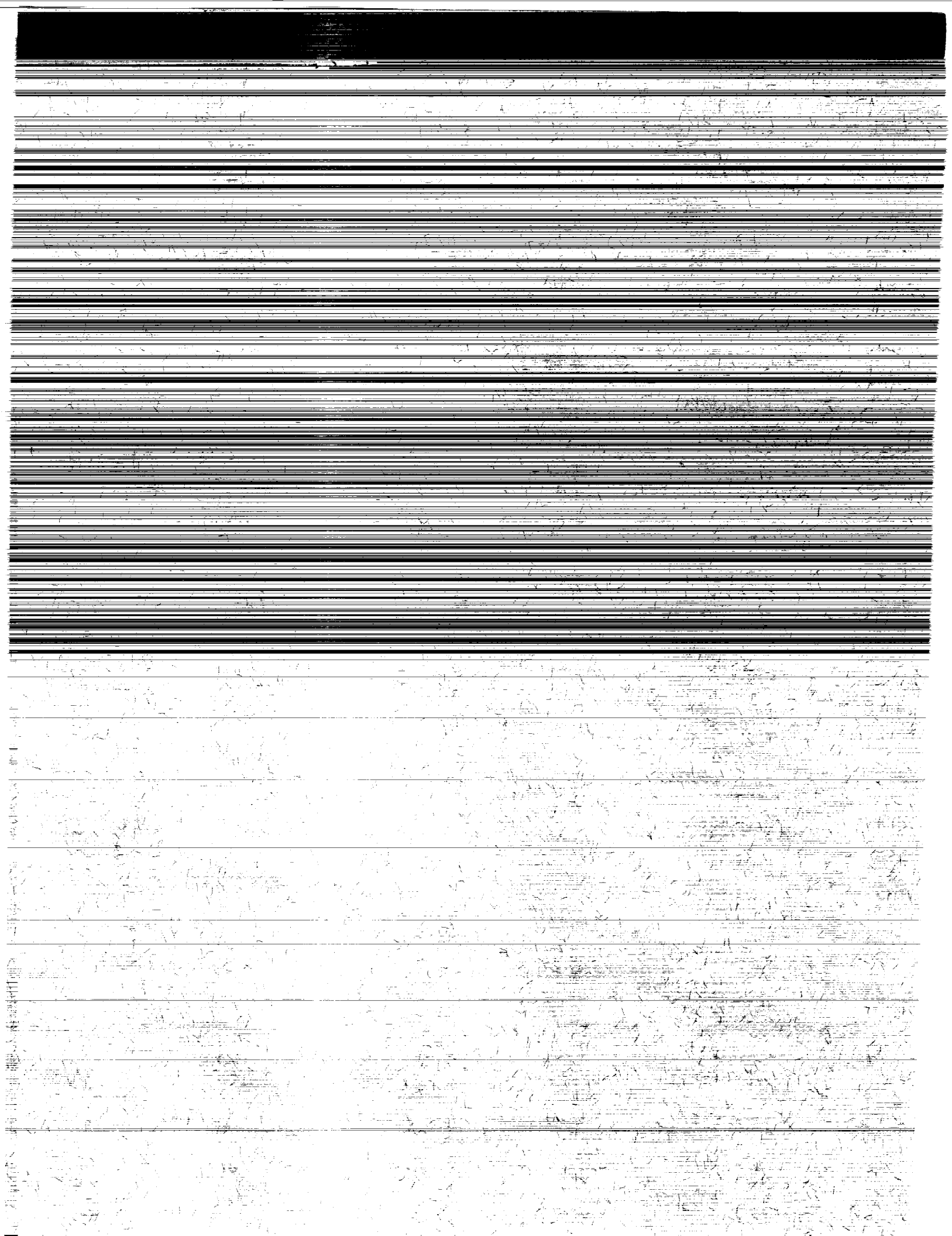
(NASA-TP-3361) ANALYSIS OF  
ELECTROMAGNETIC SCATTERING FROM  
IRREGULARLY SHAPED, THIN, METALLIC  
FLAT PLATES (NASA) 49 p

N94-16655

Unclas

H1/32 0193039

**NASA**



1993

# Analysis of Electromagnetic Scattering From Irregularly Shaped, Thin, Metallic Flat Plates

Manohar D. Deshpande  
*ViGYAN, Inc.*  
*Hampton, Virginia*

C. R. Cockrell, Fred B. Beck,  
Erik Vedeler, and Melissa B. Koch  
*Langley Research Center*  
*Hampton, Virginia*



National Aeronautics and  
Space Administration  
Office of Management  
Scientific and Technical  
Information Program



## Contents

Abstract . . . . .	1
Introduction . . . . .	1
Symbols . . . . .	2
Theory . . . . .	4
General Theory . . . . .	4
Radar Cross Section . . . . .	9
Numerical Results . . . . .	11
RCS of Hexagonal Plate . . . . .	11
RCS of Equilateral Triangular Plate . . . . .	12
RCS of Equilateral Triangular Plate With Concentric, Equilateral Triangular Hole . . . . .	12
RCS of Equilateral Triangular Plate With Inverted, Equilateral Triangular Hole . . . . .	12
RCS of Diamond-Shaped Plate . . . . .	12
Comparison of CPU Time . . . . .	13
Concluding Remarks . . . . .	13
Appendix—Description of Floppy Disk Contents . . . . .	14
References . . . . .	15
Figures . . . . .	16

PRECEDING PAGE BLANK NOT FILMED



## Abstract

*This report describes an application of the method of moments to calculate the electromagnetic scattering from irregularly shaped, thin, metallic flat plates in free space. In the present technique, an irregularly shaped plate is enclosed by a rectangle on which the surface-current density is then expressed in terms of subdomain functions by dividing the rectangle into subsections. A shape function is introduced to ensure zero current outside the patch. The surface-current density is determined using the electric field integral equation (EFIE) approach in conjunction with the method of moments, and from a knowledge of the surface-current density, the electromagnetic scattering from a plate is calculated. Using this technique, the electromagnetic scattering from (1) a hexagonal plate, (2) an equilateral triangular plate, (3) an equilateral triangular plate with a concentric, equilateral triangular hole and an inverted, equilateral triangular hole, and (4) a diamond-shaped plate is computed and compared with the numerical results obtained by using the Electromagnetic Surface Patch (ESP) code developed by Ohio State University. The numerical results compare favorably with the measurements performed on these shapes in the Langley Experimental Test Range facility.*

## Introduction

A knowledge of electromagnetic (EM) scattering from a complex-shaped metallic object is of practical interest to electromagnetic analysts and engineers. In recent years, considerable interest has developed in the EM scattering analysis of polygonal plates because a complex-shaped metallic object can always be modeled as an interconnection of these polygonal flat plates (ref. 1). An EM scattering analysis of a polygonal, metallic flat plate can be accomplished by using various numerical techniques. One of the widely used techniques is the method of moments in which a polygonal plate is first segmented into a number of rectangular or nonrectangular surface patches called *subdomains*. The unknown surface-current density on these subdomains is then determined using the electric field integral equation (EFIE) in conjunction with the method of moments.

The early work on polygonal flat plates (ref. 2) consisted of subdividing an irregularly shaped plate into a collection of curvilinear cells that were represented numerically as fourth-order polynomials. However, use of that method required a knowledge of the coordinates of a large number of points on the object, and this made the method unattractive. In another approach (refs. 3 and 4), a nonrectangular plate was viewed as an interconnection of polygonal plates. The unknown amplitudes of the surface patch modes were determined by expressing the currents on the polygonal plates in terms of nonrectangular sur-

face patch modes and using the EFIE in conjunction with the method of moments.

An Electromagnetic Surface Patch (ESP) code was developed in 1988 under NASA Grant NSG 1498 by E. H. Newman at the ElectroScience Laboratory, Ohio State University. (This code is described in a manual entitled *A User's Manual for the Electromagnetic Surface Patch Code: ESP Version IV*.) The ESP code was based on the segmentation techniques described in references 3 and 4. Even though the segmentation technique used in the ESP code completely filled the area of the nonrectangular plate, extra current modes were required at the interconnections of the polygonal plates to ensure a continuity of current. Furthermore, when nonrectangular surface patch modes were used to express the surface current, the resulting matrix would be symmetric but not of a block Toeplitz nature, and hence it would require more impedance matrix filling time. In the present work, a segmentation technique that is both symmetric and results in a block Toeplitz impedance matrix is developed to analyze the EM scattering from polygonal, thin, metallic flat plates.

In the present analysis, an irregularly shaped plate is assumed to be enclosed by a rectangle with sides equal to  $W_x$  and  $W_y$ , the maximum dimensions in the  $x$ - and  $y$ -directions, respectively. By dividing  $W_x$  into  $(M + 1)$  subdivisions and  $W_y$  into  $(N + 1)$  subdivisions, the surface-current density over

the rectangle is expressed in terms of overlapping triangular functions in the direction of current flow and a pulse function in the orthogonal direction. Zero current outside the plate is ensured by introducing a space function in the current expansion function. (A space function is equal to 1/0 if the subdomain lies inside/outside of the irregular plate.) Selecting the testing functions to be the same as the expansion functions allows the EFIE to be reduced to a matrix equation that is solved by using standard matrix-equation solver subroutines. The surface current on the plate is then used to determine EM scattering due to the plate. By using this technique, the EM scattering due to several nonrectangular plates is computed and compared with the results obtained from Newman's ESP code. The results obtained from using the present method are also compared with the experimental data measured in the Langley Experimental Test Range (ETR) facility, which is a compact range specifically designed for microwave scattering measurements. The ETR is a dual anechoic chamber with a Gregorian reflector system (ref. 5) containing a 16-ft<sup>2</sup> rolled-edge main reflector.

The measured data are provided on a floppy disk for the reader, a description of which is given in the appendix.

## Symbols

$\mathbf{A}(x, y, z)$	magnetic vector potential
$\mathbf{E}_i$	incident electric field vector
$ \mathbf{E}_i $	absolute value of incident electric field vector
$\mathbf{E}_s(x, y, z)$	scattered electric field vector
$E_{sx}$	$x$ -component of scattered field $\mathbf{E}_s$
$E_{sy}$	$y$ -component of scattered field $\mathbf{E}_s$
$E_{s\theta}$	$\theta$ -component of scattered field $\mathbf{E}_s$
$E_{s\phi}$	$\phi$ -component of scattered field $\mathbf{E}_s$
$E_{xi}, E_{yi}, E_{zi}$	$x$ -, $y$ -, and $z$ -components, respectively, of incident electric field
$E_{\theta_i}, E_{\phi_i}$	$\theta$ - and $\phi$ -components, respectively, of incident electric field
$e_x(k_x, k_y, 0)$	Fourier transform of $E_{sx}(x, y, 0)$
$e_y(k_x, k_y, 0)$	Fourier transform of $E_{sy}(x, y, 0)$
$F_{xmn}(k_x, k_y)$	Fourier transform of $P_m(x) Q_n(y)$

$F_{ymn}(k_x, k_y)$	Fourier transform of $Q_m(x) P_n(y)$
$\{FX\}$	$= \frac{\sin(k_x \Delta x/2)}{k_x \Delta x/2}$
$\{FY\}$	$= \frac{\sin(k_y \Delta y/2)}{k_y \Delta y/2}$
$\{FX1\}$	$= \frac{\sin[(\sin \theta_i \cos \phi_i)(k_0 \Delta x/2)]}{\sin \theta_i \cos \phi_i k_0 (\Delta x/2)}$
$\{FY1\}$	$= \frac{\sin[(\sin \theta_i \sin \phi_i)(k_0 \Delta y/2)]}{(\sin \theta_i \sin \phi_i)(k_0 \Delta y/2)}$
$f$	frequency, GHz
$G(x, y, z/x', y')$	free-space-scalar Green's function
$g(k_x, k_y, z/x', y')$	Fourier transform of $G(x, y, z/x', y')$
$\mathbf{H}_i$	incident magnetic field vector
$I_x(p)$	complex amplitude of $p$ th $x$ -directed subdomain current mode
$I_y(q)$	complex amplitude of $q$ th $y$ -directed subdomain current mode
$\mathbf{J}_s(x, y)$	induced surface-current density vector on plate
$J_{sx}(x, y)$	$x$ -component of $\mathbf{J}_s(x, y)$
$J_{sy}(x, y)$	$y$ -component of $\mathbf{J}_s(x, y)$
$j$	$= \sqrt{-1}$
$\mathbf{j}_s$	Fourier transform of $\mathbf{J}_s$
$j_{sx}$	$x$ -component of $\mathbf{j}_s$
$j_{sy}$	$y$ -component of $\mathbf{j}_s$
$\mathbf{k}_i$	propagation vector of plane wave
$k_x$	Fourier transform variable with respect to $x$
$k_y$	Fourier transform variable with respect to $y$
$k_z$	complex propagation constant in $z$ -direction
$k_0$	propagation constant in free space
$M + 1$	number of subdivisions in $x$ -direction
$m, n$	$(m, n)$ th subdomain of induced current
$m', n'$	$(m', n')$ th subdomain of induced current
$N + 1$	number of subdivisions in $y$ -direction



$P$	total number of $x$ -directed subdomains on plate	$Z_{xy}^{q,p'}$	mutual impedance between $q$ th $y$ -directed and $p'$ th $x$ -directed subdomain currents
$P_m(x)$	piecewise linear distribution in $x$ -direction	$Z_{yx}^{p,q'}$	mutual impedance between $p$ th $x$ -directed and $q'$ th $y$ -directed subdomain currents
$P_n(y)$	piecewise linear distribution in $y$ -direction	$Z_{yy}^{q,q'}$	mutual impedance between $q$ th and $q'$ th $y$ -directed subdomain currents
$p$	equivalent to $(m, n)$ th $x$ -directed subdomain	$\alpha, \beta$	polar coordinate variables related to $k_x, k_y$
$p'$	equivalent to $(m', n')$ th $x$ -directed subdomain	$\alpha_0$	angle between $\mathbf{E}_i$ and $\hat{\theta}_i$ , deg
$Q$	total number of $y$ -directed subdomains on plate	$\Delta x$	$= \frac{W_x}{M+1}$
$Q_m(y)$	pulse distribution in $y$ -direction	$\Delta y$	$= \frac{W_y}{N+1}$
$Q_n(x)$	pulse distribution in $x$ -direction	$\delta$	delta function
$q$	equivalent to $(m, n)$ th $y$ -directed subdomain	$\eta_0$	free-space wave impedance
$q'$	equivalent to $(m', n')$ th $y$ -directed subdomain	$\theta, \phi$	angles of scattered electromagnetic wave
$R_{xx}^{p,p'}$	real part of $Z_{xx}^{p,p'}$	$\theta_i, \phi_i$	incident angles of electromagnetic wave
$\mathbf{r}$	position vector in direction of plane wave	$\hat{\theta}_i, \hat{\phi}_i$	unit vectors along $\theta_i$ and $\phi_i$ axes, respectively, in spherical coordinate system
$S_x(m, n)$	shape function for $x$ -directed current ( $= 1$ or $0$ )	$\hat{\theta}_s, \hat{\phi}_s$	unit vectors along $\theta_s$ and $\phi_s$ axes, respectively, in spherical coordinate system
$S_y(m, n)$	shape function for $y$ -directed current ( $= 1$ or $0$ )	$\lambda_0$	wavelength in free space
$V_x^{p'}$	reaction of $p'$ th $x$ -directed subdomain testing function with $E_{xi}$	$\mu_0$	magnetic permeability of free space
$V_y^{q'}$	reaction of $q'$ th $y$ -directed subdomain testing function with $E_{yi}$	$\sigma$	total radar cross section
$W_x$	maximum dimension of plate in $x$ -direction	$\sigma_{EE}$	copolarized radar cross section when $E$ -polarized wave is transmitted
$W_y$	maximum dimension of plate in $y$ -direction	$\sigma_{EH}$	cross-polarized radar cross section when $E$ -polarized wave is transmitted
$X_{xx}^{p,p'}$	imaginary part of $Z_{xx}^{p,p'}$	$\sigma_{HE}$	cross-polarized radar cross section when $H$ -polarized wave is transmitted
$x, y, z$	Cartesian coordinates of field point		
$x', y', z'$	Cartesian coordinates of source point		
$Z_{xx}^{p,p'}$	mutual impedance between $p$ th and $p'$ th $x$ -directed subdomain currents		

$\sigma_{HH}$	copolarized radar cross section when $H$ -polarized wave is transmitted	Abbreviations:	
		EFIE	electric field integral equation
$\omega$	angular frequency, $2\pi f$	EM	electromagnetic
		ESP	Electromagnetic Surface Patch
$\nabla$	gradient operator	RCS	radar cross section

## Theory

### General Theory

Consider an irregularly shaped, infinitesimally thin plate excited by a plane wave as shown in figure 1(a). By using the representation of reference 6, the incident field with a time variation of  $e^{j\omega t}$  may be written as

$$\begin{aligned}\mathbf{E}_i(x, y, z) &= (\hat{\theta}_i E_{\theta_i} + \hat{\phi}_i E_{\phi_i}) e^{-j\mathbf{k}_i \cdot \mathbf{r}} \\ &= (\hat{\theta}_i |\mathbf{E}_i| \cos \alpha_0 + \hat{\phi}_i |\mathbf{E}_i| \sin \alpha_0) e^{-j\mathbf{k}_i \cdot \mathbf{r}}\end{aligned}\quad (1)$$

where

$$\mathbf{k}_i \cdot \mathbf{r} = -k_0 \sin \theta_i (x \cos \phi_i + y \sin \phi_i)$$

and  $k_0$  is the free-space wave number. From equation (1), the  $x$ -,  $y$ -, and  $z$ -components of the incident field may be written, respectively, as

$$\begin{aligned}E_{xi} &= E_{\theta_i} \cos \theta_i \cos \phi_i - E_{\phi_i} \sin \phi_i \\ E_{yi} &= E_{\theta_i} \cos \theta_i \sin \phi_i + E_{\phi_i} \cos \phi_i \\ E_{zi} &= -E_{\theta_i} \sin \theta_i\end{aligned}\quad (2)$$

The corresponding magnetic field components are obtained through

$$\mathbf{H}_i = \frac{1}{\eta_0} \mathbf{k}_i \times \mathbf{E}_i \quad (3)$$

where  $\eta_0$  is the free-space impedance. The incident field with  $E_{\theta_i} \neq 0$ ,  $E_{\phi_i} = 0$  (i.e.,  $\alpha_0 = 0^\circ$ ) is called the *H-polarized wave* and with  $E_{\theta_i} = 0$ ,  $E_{\phi_i} \neq 0$  (i.e.,  $\alpha_0 = 90^\circ$ ) is called the *E-polarized wave*.

Let  $\mathbf{J}_s(x, y)$  be the induced surface-current density on the plate. The electromagnetic field due to  $\mathbf{J}_s(x, y)$  located in the  $z = 0$  plane may be obtained from the magnetic vector potential  $\mathbf{A}(x, y, z)$  as

$$\mathbf{H}_s(x, y, z) = \frac{1}{\mu_0} \nabla \times \mathbf{A}(x, y, z) \quad (4)$$

$$\mathbf{E}_s(x, y, z) = \frac{-j\omega}{k_0^2} \left\{ k_0^2 \mathbf{A}(x, y, z) + \nabla [\nabla \cdot \mathbf{A}(x, y, z)] \right\} \quad (5)$$

where  $\mu_0$  is the permeability of the medium. The vector potential  $\mathbf{A}(x, y, z)$  in equations (4) and (5) satisfies the wave equation

$$\nabla^2 \mathbf{A}(x, y, z) + k_0^2 \mathbf{A}(x, y, z) = -\mu_0 \mathbf{J}_s(x', y') \quad (6)$$

If  $G(x, y, z/x', y')$  is the free-space-scalar Green's function, the magnetic vector potential  $\mathbf{A}(x, y, z)$  is obtained from

$$\mathbf{A}(x, y, z) = \iint \mathbf{J}_s(x', y') G(x, y, z/x', y') dx' dy' \quad (7)$$

where  $G(x, y, z/x', y')$  satisfies

$$(\nabla^2 + k_0^2) G(x, y, z/x', y') = -\mu_0 \delta(x - x') \delta(y - y') \delta(z) \quad (8)$$

The solution of equation (8) in the  $(k_x, k_y)$  domain may be written as (ref. 7)

$$G(x, y, z/x', y') = \frac{1}{(2\pi)^2} \int_{k_x=-\infty}^{\infty} dk_x \int_{k_y=-\infty}^{\infty} g(k_x, k_y, z/x', y') e^{jk_x x + jk_y y} dk_y \quad (9)$$

where

$$g(k_x, k_y, z/x', y') = \frac{-j\mu}{2k_z} e^{-jk_x x' - jk_y y'} e^{\pm jk_z z}$$

$$k_z = \begin{cases} \sqrt{k_0^2 - k_x^2 - k_y^2} & (k_x^2 + k_y^2 \leq k_0^2) \\ -j\sqrt{k_x^2 + k_y^2 - k_0^2} & (k_x^2 + k_y^2 \geq k_0^2) \end{cases}$$

and the + and - signs in the exponential are used for  $z < 0$  and  $z > 0$ , respectively. Substituting equation (9) into equation (7) gives the magnetic vector potential

$$\mathbf{A}(x, y, 0) = \frac{-j\mu_0}{(2\pi)^2} \int_{k_x=-\infty}^{\infty} dk_x \int_{k_y=-\infty}^{\infty} \frac{\mathbf{j}_s(k_x, k_y)}{2k_z} e^{jk_x x + jk_y y} dk_y \quad (10)$$

where

$$\begin{aligned} \mathbf{j}_s(k_x, k_y) &= \hat{x}j_{sx} + \hat{y}j_{sy} \\ &= \int dx' \int dy' \mathbf{J}_s(x', y') e^{-jk_x x' - jk_y y'} \end{aligned} \quad (11)$$

Substituting equation (12) into equation (5) allows us to write the scattered tangential components of the electric field over the plate due to the induced currents as

$$E_{sx}(x, y, 0) = \frac{-\omega\mu_0}{(2\pi)^2 k_0^2} \int_{k_x=-\infty}^{\infty} dk_x \int_{k_y=-\infty}^{\infty} \left[ (k_0^2 - k_x^2) j_{sx}(k_x, k_y) - k_x k_y j_{sy}(k_x, k_y) \right] \times e^{jk_x x + jk_y y} \frac{dk_y}{2k_z} \quad (12)$$

$$\begin{aligned} E_{sy}(x, y, 0) &= \frac{-\omega\mu_0}{(2\pi)^2 k_0^2} \int_{k_x=-\infty}^{\infty} dk_x \int_{k_y=-\infty}^{\infty} \left[ (-k_x k_y) j_{sx}(k_x, k_y) + (k_0^2 - k_y^2) j_{sy}(k_x, k_y) \right] \\ &\quad \times e^{jk_x x + jk_y y} \frac{dk_y}{2k_z} \end{aligned} \quad (13)$$

Subjecting the total tangential electric field on the plate to zero gives the following equations

$$E_{sx} + E_{xi} e^{-j(\mathbf{k}_i \cdot \mathbf{r})} = 0$$

$$E_{sy} + E_{yi} e^{-j(\mathbf{k}_i \cdot \mathbf{r})} = 0$$

Substituting equations (2), (12), and (13) into the above equations gives the following integral equations with surface current as an unknown variable:

$$\frac{\omega\mu_0}{(2\pi)^2 k_0^2} \int_{k_x=-\infty}^{\infty} dk_x \int_{k_y=-\infty}^{\infty} \left[ (k_0^2 - k_x^2) j_{sx}(k_x, k_y) - k_x k_y j_{sy}(k_x, k_y) \right] \times e^{jk_x x + jk_y y} \frac{dk_y}{2k_z} = E_{xi} e^{-j\mathbf{k}_i \cdot \mathbf{r}} \quad (14)$$

$$\frac{\omega\mu_0}{(2\pi)^2 k_0^2} \int_{k_x=-\infty}^{\infty} dk_x \int_{k_y=-\infty}^{\infty} \left[ (-k_x k_y) j_{sx}(k_x, k_y) + (k_0^2 - k_y^2) j_{sy}(k_x, k_y) \right] \times e^{jk_x x + jk_y y} \frac{dk_y}{2k_z} = E_{yi} e^{-j\mathbf{k}_i \cdot \mathbf{r}} \quad (15)$$

With the aid of figure 1(b), the surface-current density distributions can be expressed as

$$J_{sx}(x, y) = \sum_{m=1}^M \sum_{n=1}^{N+1} S_x(m, n) I_x(m, n) P_m(x) Q_n(y) \quad (16a)$$

and

$$J_{sy}(x, y) = \sum_{m=1}^{M+1} \sum_{n=1}^N S_y(m, n) I_y(m, n) Q_m(x) P_n(y) \quad (16b)$$

where  $I_x(m, n)$  and  $I_y(m, n)$  are the unknown current amplitudes and

$$P_m(x) = \begin{cases} 1 - \frac{x_m - x}{\Delta x} & ((x_m - \Delta x) \leq x \leq x_m) \\ 1 - \frac{x - x_m}{\Delta x} & (x_m \leq x \leq (x_m + \Delta x)) \\ 0 & (\text{Otherwise}) \end{cases}$$

$$Q_n(y) = \begin{cases} 1 & (n-1)\Delta y \leq y \leq n \Delta y \\ 0 & (\text{Otherwise}) \end{cases}$$

If the  $(m, n)$ th cell lies inside the plate, then

$$\left. \begin{matrix} S_x(m, n) \\ S_y(m, n) \end{matrix} \right\} = 1$$

Otherwise,

$$\left. \begin{matrix} S_x(m, n) \\ S_y(m, n) \end{matrix} \right\} = 0$$

Also,

$$\Delta x = \frac{W_x}{M+1}$$

$$\Delta y = \frac{W_y}{N+1}$$

Here,  $W_x$  and  $W_y$  are the maximum dimensions of the plate in the  $x$ - and  $y$ -directions, respectively. The  $(m, n)$ th cell is considered to be inside the plate if the area occupied by the plate is more than 50 percent of the cell area.

Using equation (11) allows us to write the Fourier transform of the patch current as

$$j_{sx}(k_x, k_y) = \sum_{m=1}^M \sum_{n=1}^{N+1} S_x(m, n) I_x(m, n) F_{xmn}(k_x, k_y) \quad (17a)$$

$$j_{sy}(k_x, k_y) = \sum_{m=1}^{M+1} \sum_{n=1}^N S_y(m, n) I_y(m, n) F_{ymn}(k_x, k_y) \quad (17b)$$

where

$$\begin{aligned}
F_{xmn}(k_x, k_y) &= \Delta x \Delta y \{FY\} \{FX\}^2 \exp \left[ jk_x \left( \frac{W_x}{2} - x_m \right) + jk_y \left( \frac{W_y}{2} - y_n + \frac{\Delta y}{2} \right) \right] \\
F_{ymn}(k_x, k_y) &= \Delta x \Delta y \{FY\}^2 \{FX\} \exp \left[ jk_x \left( \frac{W_x}{2} - x_m + \frac{\Delta x}{2} \right) + jk_y \left( \frac{W_y}{2} - y_n \right) \right] \\
\{FX\} &= \frac{\sin(k_x \Delta x/2)}{k_x \Delta x/2} \\
\{FY\} &= \frac{\sin(k_y \Delta y/2)}{k_y \Delta y/2}
\end{aligned}$$

With reference to figure 1(b), the double summation with respect to  $m$  and  $n$  in equation (17) can be represented by a single summation with respect to  $p$  or  $q$ . If  $P$  and  $Q$  are the maximum numbers of  $x$ - and  $y$ -domain subcells, respectively, on the plate, then equations (17) may be rewritten as

$$j_{sx}(k_x, k_y) = \sum_{p=1}^P I_x(p) F_{xp}(k_x, k_y) \quad (18a)$$

$$j_{sy}(k_x, k_y) = \sum_{q=1}^Q I_y(q) F_{yq}(k_x, k_y) \quad (18b)$$

Substitution of equations (18) into equations (14) and (15) and use of the method of moments yields

$$\sum_{p=1}^P I_x(p) Z_{xx}^{p,p'} + \sum_{q=1}^Q I_y(q) Z_{xy}^{q,p'} = V_x^{p'} \quad (19)$$

$$\sum_{p=1}^P I_x(p) Z_{yx}^{p,q'} + \sum_{q=1}^Q I_y(q) Z_{yy}^{q,q'} = V_y^{q'} \quad (20)$$

where  $p' = 1, 2, \dots, P$ ,  $q' = 1, 2, \dots, Q$ , and

$$Z_{xx}^{p,p'} = \frac{\omega \mu_0}{(2\pi)^2 k_0^2} \int_{k_x=-\infty}^{\infty} \int_{k_y=-\infty}^{\infty} \frac{k_0^2 - k_x^2}{2k_z} F_{xp}(k_x, k_y) F_{xp'}^*(k_x, k_y) dk_x dk_y \quad (21)$$

$$Z_{xy}^{q,p'} = \frac{\omega \mu_0}{(2\pi)^2 k_0^2} \int_{k_x=-\infty}^{\infty} \int_{k_y=-\infty}^{\infty} \frac{-k_x k_y}{2k_z} F_{yq}(k_x, k_y) F_{xp'}^*(k_x, k_y) dk_x dk_y \quad (22)$$

$$Z_{yx}^{p,q'} = \frac{\omega \mu_0}{(2\pi)^2 k_0^2} \int_{k_x=-\infty}^{\infty} \int_{k_y=-\infty}^{\infty} \frac{-k_x k_y}{2k_z} F_{xp}(k_x, k_y) F_{yq'}^*(k_x, k_y) dk_x dk_y \quad (23)$$

$$Z_{yy}^{q,q'} = \frac{\omega \mu_0}{(2\pi)^2 k_0^2} \int_{k_x=-\infty}^{\infty} \int_{k_y=-\infty}^{\infty} \frac{k_0^2 - k_y^2}{2k_z} F_{yq}(k_x, k_y) F_{yq'}^*(k_x, k_y) dk_x dk_y \quad (24)$$

$$V_x^{p'} = \iint E_{xi} e^{-j\mathbf{k}_i \cdot \mathbf{r}} P_{m'}(x') Q_{n'}(y') dx' dy' \quad (25)$$

$$V_y^{q'} = \iint E_{yi} e^{-j\mathbf{k}_i \cdot \mathbf{r}} Q_{m'}(x') P_{n'}(y') dx' dy' \quad (26)$$

In equations (21)–(24), the superscript \* indicates a complex conjugate. Using the expressions for  $F_{xp}$  and  $F_{yq}$  with the substitutions  $k_x = k_0 \beta \cos \alpha$  and  $k_y = k_0 \beta \sin \alpha$  allows equations (21), (22), (23), and (24) to be written, respectively, in terms of the new variables  $(\alpha, \beta)$  as

$$Z_{xx}^{p,p'} = \frac{\eta_0 k_0^2 \Delta^2 x \Delta^2 y}{\pi^2} \int_{\beta=0}^{\infty} \beta d\beta \int_{\alpha=0}^{\pi/2} \frac{1 - \beta^2 \cos^2 \alpha}{2\sqrt{1 - \beta^2}} \{FY\}^2 \{FX\}^4 \times \cos[k_0(x_{p,p'}) \beta \cos \alpha] \cos[k_0(y_{p,p'}) \beta \sin \alpha] d\alpha \quad (27)$$

where  $x_{p,p'} = x_m - x_{m'}$  and  $y_{p,p'} = y_n - y_{n'}$ ,

$$Z_{xy}^{q,p'} = \frac{\eta_0 k_0^2 \Delta^2 x \Delta^2 y}{\pi^2} \int_{\beta=0}^{\infty} \beta d\beta \int_{\alpha=0}^{\pi/2} \frac{\beta^2 \cos \alpha \sin \alpha}{2\sqrt{1 - \beta^2}} \{FY\}^3 \{FX\}^3 \times \sin[k_0(x_{q,p'}) \beta \cos \alpha] \sin[k_0(y_{q,p'}) \beta \sin \alpha] d\alpha \quad (28)$$

where  $x_{q,p'} = x_m - x_{m'} + \frac{\Delta x}{2}$  and  $y_{q,p'} = y_n - y_{n'} - \frac{\Delta y}{2}$ ,

$$Z_{yx}^{p,q'} = Z_{xy}^{q,p'} \quad (29)$$

and

$$Z_{yy}^{q,q'} = \frac{\eta_0 k_0^2 \Delta^2 x \Delta^2 y}{\pi^2} \int_{\beta=0}^{\infty} \beta d\beta \int_{\alpha=0}^{\pi/2} \frac{1 - \beta^2 \sin^2 \alpha}{2\sqrt{1 - \beta^2}} \{FY\}^4 \{FX\}^2 \times \cos[k_0(x_{q,q'}) \beta \cos \alpha] \cos[k_0(y_{q,q'}) \beta \sin \alpha] d\alpha \quad (30)$$

where  $x_{q,q'} = x_m - x_{m'}$  and  $y_{q,q'} = y_n - y_{n'}$ . In deriving equations (27)–(30), the even and odd properties of the integrands have been utilized.

Integrating equations (25) and (26) with respect to  $x'$  and  $y'$  gives, respectively,

$$V_x^{p'} = \Delta x \Delta y E_{xi} \{FY1\} \{FX1\}^2 \exp \left[ jk_0 \left( x_{m'} - \frac{W_x}{2} \right) \sin \theta_i \cos \phi_i \right] \times \exp \left[ jk_0 \left( y_{n'} - \frac{W_y}{2} - \frac{\Delta y}{2} \right) \sin \theta_i \sin \phi_i \right] \quad (31)$$

and

$$V_y^{q'} = \Delta x \Delta y E_{yi} \{FY1\}^2 \{FX1\} \exp \left[ jk_0 \left( x_{m'} - \frac{W_x}{2} - \frac{\Delta x}{2} \right) \sin \theta_i \cos \phi_i \right] \times \exp \left[ jk_0 \left( y_{n'} - \frac{W_y}{2} \right) \sin \theta_i \sin \phi_i \right] \quad (32)$$

where  $\{FX1\}$  is obtained from  $\{FX\}$  by replacing  $\beta \cos \alpha$  with  $\sin \theta_i \cos \phi_i$ , and  $\{FY1\}$  is obtained from  $\{FY\}$  by replacing  $\beta \sin \alpha$  with  $\sin \theta_i \sin \phi_i$ .

The elements  $Z_{xx}^{p,p'}$ ,  $Z_{xy}^{q,p'}$ , etc., of the coefficient matrix are determined from equations (27)–(30) by using gauss-quadrature numerical integration techniques. The presence of  $\sqrt{1 - \beta^2}$  in the denominators of the integrands of equations (27)–(30) causes numerical difficulty around  $\beta = 1$ . However, this is avoided by splitting the  $\beta$  integration into two parts: the first part consists of integration from  $\beta = 0$  to 1, and the second part consists of integration from  $\beta = 1$  to  $\infty$ . When  $\beta$  is replaced by  $\sin \zeta$  in the first part and by  $\cosh \zeta$  in the second part, equation (27) becomes

$$Z_{xx}^{p,p'} = R_{xx}^{p,p'} + jX_{xx}^{p,p'} \quad (33)$$

where

$$R_{xx}^{p,p'} = \frac{\eta_0 k_0^2 \Delta^2 x \Delta^2 y}{2(\pi)^2} \int_{\zeta=0}^{\pi/2} \sin \zeta d\zeta \int_{\alpha=0}^{\pi/2} (1 - \sin^2 \zeta \cos^2 \alpha) \{FY\}^2 \{FX\}^4 \\ \times \cos[k_0(x_{p,p'}) \sin \zeta \cos \alpha] \cos[k_0(y_{p,p'}) \sin \zeta \sin \alpha] d\alpha$$

$$X_{xx}^{p,p'} = \frac{j\eta_0 k_0^2 \Delta^2 x \Delta^2 y}{2(\pi)^2} \int_{\zeta=0}^{\infty} \cosh \zeta d\zeta \int_{\alpha=0}^{\pi/2} (1 - \cosh^2 \zeta \cos^2 \alpha) \{FY\}^2 \{FX\}^4 \\ \times \cos[k_0(x_{p,p'}) \cosh \zeta \cos \alpha] \cos[k_0(y_{p,p'}) \cosh \zeta \sin \alpha] d\alpha$$

where  $\{FX\}$  and  $\{FY\}$  in the equations for  $R_{xx}^{p,p'}$  and  $X_{xx}^{p,p'}$  are, as defined earlier, with the appropriate change of variables.

Similarly, the singularities due to the presence of  $\sqrt{1 - \beta^2}$  in the denominators of equations (28)–(30) are removed and thus yield expressions analogous to equation (33).

Equations (19) and (20) can now be solved for  $I_x(p)$  and  $I_y(q)$  either by using the matrix inversion method or by decomposing the impedance matrix into lower and upper triangular matrices. We show later that the method of triangular decomposition (ref. 8) is preferred over the matrix inversion method because the former takes less central processing unit (CPU) time.

### Radar Cross Section

The radiation field due to the plate is given by (ref. 9)

$$E_{\theta s} = [e_x(k_x, k_y, 0) \cos \phi + e_y(k_x, k_y, 0) \sin \phi] \frac{jk_0}{2\pi r} e^{-jk_0 r} \quad (34)$$

$$E_{\phi s} = [e_y(k_x, k_y, 0) \cos \phi - e_x(k_x, k_y, 0) \sin \phi] \cos \theta \frac{jk_0}{2\pi r} e^{-jk_0 r} \quad (35)$$

where  $e_x(k_x, k_y, 0)$  and  $e_y(k_x, k_y, 0)$  are the Fourier transforms of the tangential electric field components at the interface  $z = 0$  (obtained from eq. (13)) and are given, respectively, as

$$e_x(k_x, k_y, 0) = \frac{-\omega\mu_0}{k_0^2} \frac{[(k_0^2 - k_x^2) j_{sx}(k_x, k_y) - k_x k_y j_{sy}(k_x, k_y)]}{2k_z} \quad (36)$$

and

$$e_y(k_x, k_y, 0) = \frac{-\omega\mu_0}{k_0^2} \frac{[-k_x k_y j_{sx}(k_x, k_y) + (k_0^2 - k_y^2) j_{sy}(k_x, k_y)]}{2k_z} \quad (37)$$

Substituting equations (36) and (37) into equations (34) and (35) gives, respectively,

$$E_{s\theta} = \frac{-\omega\mu}{k_0^2} [j_{sx}(k_x, k_y) \{1\} + j_{sy}(k_x, k_y) \{2\}] \frac{jk_0}{2\pi r} e^{-jk_0 r} \quad (38)$$

and

$$E_{s\phi} = \frac{-\omega\mu}{k_0^2} [j_{sx}(k_x, k_y) \{3\} + j_{sy}(k_x, k_y) \{4\}] \cos \theta \frac{jk_0}{2\pi r} e^{-jk_0 r} \quad (39)$$

where

$$\{1\} = \frac{k_0^2 - k_x^2}{2k_z} \cos \phi - \frac{k_x k_y}{2k_z} \sin \phi$$

$$\begin{aligned}\{2\} &= \frac{-k_x k_y}{2k_z} \cos \phi + \frac{k_0^2 - k_y^2}{2k_z} \sin \phi \\ \{3\} &= \frac{-k_x k_y}{2k_z} \cos \phi - \frac{k_0^2 - k_x^2}{2k_z} \sin \phi \\ \{4\} &= \frac{k_0^2 - k_y^2}{2k_z} \cos \phi + \frac{k_x k_y}{2k_z} \sin \phi\end{aligned}$$

By substituting  $k_x = k_0 \sin \theta \cos \phi$  and  $k_y = k_0 \sin \theta \sin \phi$ , the above equations reduce to

$$\begin{aligned}\{1\} &= \frac{k_0}{2} \cos \phi \cos \theta \\ \{2\} &= \frac{k_0}{2} \sin \phi \cos \theta \\ \{3\} &= \frac{-k_0 \sin \phi}{2 \cos \theta} \\ \{4\} &= \frac{k_0 \cos \phi}{2 \cos \theta}\end{aligned}$$

By using the above expressions, the scattered electric field components are obtained as

$$E_{s\theta} = \frac{-\eta_0 \cos \theta}{2} [j_{sx}(k_x, k_y) \cos \phi + j_{sy}(k_x, k_y) \sin \phi] \frac{jk_0}{2\pi r} e^{-jk_0 r} \quad (40)$$

$$E_{s\phi} = \frac{-\eta_0}{2} [j_{sy}(k_x, k_y) \cos \phi - j_{sx}(k_x, k_y) \sin \phi] \frac{jk_0}{2\pi r} e^{-jk_0 r} \quad (41)$$

After substituting for  $j_x$  and  $j_y$  and performing a few mathematical manipulations, the scattered field components are written as

$$\begin{aligned}E_{s\theta} &= \frac{-j\eta_0 k_0 \Delta x k_0 \Delta y \lambda_0}{4\pi \sqrt{\pi}} \frac{e^{-jk_0 r}}{2\sqrt{\pi r}} \cos \theta \left\{ \left[ \sum_{p=1}^P I_x(p) \frac{F_{xp}(k_x, k_y)}{\Delta x \Delta y} \cos \phi \right] \right. \\ &\quad \left. + \left[ \sum_{q=1}^Q I_y(q) \frac{F_{yq}(k_x, k_y)}{\Delta x \Delta y} \sin \phi \right] \right\} \quad (42)\end{aligned}$$

$$E_{s\phi} = \frac{-j\eta_0 k_0 \Delta x k_0 \Delta y \lambda_0}{4\pi \sqrt{\pi}} \frac{e^{-jk_0 r}}{2\sqrt{\pi r}} \left\{ \left[ \sum_{q=1}^Q I_y(q) \frac{F_{yq}(k_x, k_y)}{\Delta x \Delta y} \cos \phi \right] - \left[ \sum_{p=1}^P I_x(p) \frac{F_{xp}(k_x, k_y)}{\Delta x \Delta y} \sin \phi \right] \right\} \quad (43)$$

In equations (42) and (43),  $F_{xp}(k_x, k_y)$  and  $F_{yq}(k_x, k_y)$  are calculated at  $k_x = -k_0 \sin \theta \cos \phi$  and  $k_y = -k_0 \sin \theta \sin \phi$ . The radar cross section of the plate, as defined in reference 10, is then obtained from

$$\sigma = \lim_{r \rightarrow \infty} 4\pi r^2 \frac{|\mathbf{E}_s|^2}{|\mathbf{E}_i|^2} \quad (44)$$

where

$$\begin{aligned}|\mathbf{E}_s|^2 &= |E_{s\theta}|^2 + |E_{s\phi}|^2 \\ |\mathbf{E}_i|^2 &= |E_{\theta_i}|^2 + |E_{\phi_i}|^2\end{aligned}$$

The radar cross section defined in equation (44) is the total monostatic radar cross section (RCS) of an object. However, in most of the measurement, either  $E$ -polarized or  $H$ -polarized waves are transmitted and the



$E$ -polarized and  $H$ -polarized scattered far fields are measured separately. In order to compare the calculated results with the measurement, the radar cross section may be defined as

$$\sigma_{HH} = \lim_{r \rightarrow \infty} 4\pi r^2 \frac{|E_{s\theta}|^2}{|E_{\theta_i}|^2} \quad (45a)$$

$$\sigma_{HE} = \lim_{r \rightarrow \infty} 4\pi r^2 \frac{|E_{s\phi}|^2}{|E_{\theta_i}|^2} \quad (45b)$$

$$\sigma_{EH} = \lim_{r \rightarrow \infty} 4\pi r^2 \frac{|E_{s\theta}|^2}{|E_{\phi_i}|^2} \quad (45c)$$

$$\sigma_{EE} = \lim_{r \rightarrow \infty} 4\pi r^2 \frac{|E_{s\phi}|^2}{|E_{\phi_i}|^2} \quad (45d)$$

## Numerical Results

In this section the RCS of nonrectangular, thin metallic plates is calculated by using equations (44) and (45). To validate the present formulation, the RCS computed by using equation (44) is compared with (1) the RCS computed by using Newman's ESP code and (2) the RCS measured in the Langley Experimental Test Range facility.

### RCS of Hexagonal Plate

As a first example, a hexagonal plate with  $a = 2.074$  cm, as shown in figure 2, is considered. To study the edge behavior, the induced current densities along the  $XX$ - and  $YY$ -planes, as shown in figure 2, are calculated using the present method and are plotted in figure 3 for  $E$ -polarized ( $\alpha_0 = 90^\circ$ ) and  $H$ -polarized ( $\alpha_0 = 0^\circ$ ) incident waves. Figure 3 shows that the normal and tangential components of the current to an edge tend to behave as expected; i.e., the normal component of the current to an edge goes to 0 and the tangential component to an edge approaches  $\infty$ . Figure 3 also shows that  $M = N \geq 19$  gives stable values of the current densities.

Furthermore, to establish the convergence of the method, monostatic RCS's of a hexagonal plate using equation (44) are calculated as a function of angle of incidence  $\theta_i$  for  $M = N = 15, 19, 21$ , and 23 and are presented in figure 4. In figure 4(a),  $0^\circ \leq \theta_i \leq 90^\circ$  for  $\phi_i = 0^\circ$  or  $180^\circ$  indicates the  $XZ$ -plane. Similarly, in figure 4(c),  $0^\circ \leq \theta_i \leq 90^\circ$  for  $\phi_i = -90^\circ$  or  $90^\circ$  indicates the  $YZ$ -plane. Because all RCS calculations in this report are made for the  $XZ$ -,  $YZ$ -, and  $XY$ -planes, this notation is followed throughout in this report. From figure 4 we can conclude that  $M = N \geq 19$  (which corresponds to

the subdomain size  $< \lambda_0/10$ ) gives reasonably stable results.

Large values of  $M$  and  $N$  are required to obtain stable results when a flat plate is illuminated by a plane wave at the grazing angle because of a rapid variation of the phase of incident electric field along the plate surface. To get the quantitative estimation of the stability for grazing incidence, the RCS of the hexagonal plate shown in figure 2 is calculated as a function of  $\phi_i$  for  $\theta_i = 90^\circ$  and is shown in figure 5.

The validity and accuracy of the present formulation are compared with measured results and with the results obtained by the Electromagnetic Surface Patch (ESP) code in figure 6 for parametric values given in the figure. For the measurement of the RCS, a hexagonal plate with dimensions shown in figure 2 with a thickness equal to 0.16 cm was fabricated and the RCS was measured in the Langley Experimental Test Range facility. While using the ESP code, the number of modes selected was equal to 511, whereas the number of modes used for the present method was 524. Figures 3–6 show that the RCS calculations of this paper compare reasonably well with the measurements and numerical results obtained from the ESP code.

Figure 7 shows the RCS of the hexagonal plate that was calculated for grazing incidence by using the present formulation along with the measured data and results obtained using the ESP code. According to figure 7, the present method shows good agreement with the measured data for the incidence angles normal to the edges of the plate. However, for incidence angles along the corners of a plate, a disagreement occurs between the two results which may be attributed to inadequate modeling of the corners.

### RCS of Equilateral Triangular Plate

As a second example, an equilateral triangular plate with  $a = 5.08$  cm is considered, as shown in figure 8. Monostatic RCS's of the plate are calculated as a function of the angle of incidence  $\theta_i$  and are shown in figure 9 for parametric values given in this figure. From this figure, we again conclude that  $M = N \geq 19$  gives stable results for the triangular plate. From these values of  $M$  and  $N$  and because the hexagonal and equilateral triangular plates considered so far in this paper have dimensions around  $2\lambda_0$ , one also can conclude that a subcell size of approximately  $\lambda/10$  is sufficient for obtaining stable results. Also, because all the plates considered in this paper have maximum dimensions of approximately  $2\lambda_0$ , all future calculations are performed using  $M = N = 19$ . However, for larger sized plates (larger than  $2\lambda_0$ ), larger values of  $M$  and  $N$  are required for convergence in accord with the  $\lambda/10$  sub-cell criterion.

For parametric values given in figure 10, the RCS of the triangular plate is calculated by using the present method and is compared both with the RCS computed by using the ESP code and with the RCS measured in the Langley Experimental Test Range facility. The RCS of the triangular plate for grazing incidence is also calculated and presented in figure 11. From these figures we can conclude that the RCS predicted by the present method is in good agreement with both the measured data and the results obtained from the ESP code. Note in the results shown above that the number of modes selected for the ESP code was 312, whereas the number of modes  $P + Q$  for the present method was 324. Because of the unavailability of measured data, the results in figures 10(a) and 11 cannot be compared with measurements.

To validate the present technique over a wide frequency band, monostatic RCS's of the triangular plate shown in figure 8 are calculated for a fixed angle of incidence as a function of frequency, and these are presented in figure 12 along with the measured data and the results obtained using the ESP code. The results obtained by using both methods (the ESP code and the present method) compare very well with the measurements.

### RCS of Equilateral Triangular Plate With Concentric, Equilateral Triangular Hole

An equilateral triangular plate with a concentric, equilateral triangular hole as shown in figure 13 with  $a = 5.08$  cm and  $b = 2.54$  cm is considered here as a third example. For the parametric values given

in figures 14 and 15, the RCS's of this plate are calculated by using the present method along with the results obtained from the ESP code and the measured data. One can observe that the present method gives RCS estimates that are comparable with the measured data and with the ESP-code calculation.

To compare frequency dependencies, the monostatic RCS's of the plate shown in figure 13 are calculated for two angles of incidence ( $\theta_i = 90^\circ, \phi_i = 90^\circ$  and  $\theta_i = 90^\circ, \phi_i = -90^\circ$ ) as a function of frequency, and these data are presented in figure 16 along with measured and calculated results from the ESP code. For the incidence angle  $\theta_i = 90^\circ, \phi_i = 90^\circ$  (the incidence on the tip), the predicted RCS's are comparable with the other results. However, for the incidence angle  $\theta_i = 90^\circ, \phi_i = -90^\circ$  (the edge on incidence), the nulls and peaks predicted by the present method are shifted in frequency from those observed in the measured data and in the results obtained from the ESP code. Note in these calculations that the number of modes used for the present method was 217 and the number of modes used for the ESP code was marginally smaller than 217.

### RCS of Equilateral Triangular Plate With Inverted, Equilateral Triangular Hole

An equilateral triangular plate with an inverted, equilateral triangular hole as shown in figure 17 is considered next. Monostatic RCS's computed using the present method for various angles of incidence and polarization are presented in figures 18 and 19 and compared with the results obtained from the ESP code. The number of modes used in both methods was the same. The agreement between the two methods was reasonably good. Because of the unavailability of experimental results for this case, the results shown in figures 18 and 19 could not be compared with the measured data.

The monostatic RCS's of the equilateral triangular plate with an inverted equilateral triangular hole as a function of frequency for a given angle of incidence are calculated by using the present method and are presented in figure 20 along with the results obtained from the ESP code. Good agreement was observed between the results of both methods.

### RCS of Diamond-Shaped Plate

By using the present formulation, the RCS's of a diamond-shaped plate as shown in figure 21 are calculated and presented in figures 22 and 23 along with measured data and the results obtained from

the ESP code. Again, the agreement among the techniques and measurements is quite good. The number of modes for the two methods was again selected to be the same.

### Comparison of CPU Time

From the results presented so far, the present method predicts the RCS of a polygonal plate with reasonable accuracy. The number of modes required to achieve this accuracy is slightly higher than the number of modes required by the ESP code for the same accuracy. This agreement is due to the fact that the edge conditions on the surface currents are not explicitly taken into account in the present formulation. To see the merits of the present method, one must compare the CPU time required to run the present code with the CPU time required by the ESP code. For a CPU time comparison, the RCS of the hexagonal plate shown in figure 2 is calculated by using the ESP code and the present method. The CPU time required by both methods is calculated as a function of the number of patch current modes and is plotted in figure 24. For these time comparisons, both codes were run on a Sun SPARCstation.

As seen in figure 24, the present method with triangular decomposition techniques takes considerably less CPU time than the ESP code. This is mainly due to the block Toeplitz nature of the impedance matrix in the present method. Because the edge conditions on the surface currents are not explicitly taken into account, the present method requires more modes than the ESP code for reasonably accurate results. However, from the earlier comparisons of the results obtained by both methods, the difference between the number of modes used for the present method and the ESP code is marginal. (The present method requires 524 modes as compared with 511 modes required by the ESP code.) The marginal increase in the number of modes for the present method may still be preferred from the CPU time consideration.

Figure 24 also gives the CPU time in seconds as required by the present method using the matrix inversion method and the matrix triangular decomposition method. Figure 24 shows that the matrix inversion method takes a much longer CPU time than that taken by the matrix decomposition method.

### Concluding Remarks

The method of moments has been described to determine the monostatic radar cross section (RCS) of irregularly shaped, thin, metallic flat plates in free space. The surface-current density on an irregularly shaped plate has been expressed in terms of rectangular subdomain functions by enclosing the plate by a rectangle and dividing the rectangle into rectangular subdomains. A shape function has been used to ensure zero current outside the arbitrarily shaped plate. The electric field integral equation (EFIE) has been used in conjunction with the method of moments to determine the surface-current density on the irregularly shaped plate. The monostatic RCS's of (1) a hexagonal plate, (2) an equilateral triangular plate, (3) an equilateral triangular plate with a concentric, equilateral triangular hole and an inverted, equilateral triangular hole, and (4) a diamond-shaped plate have been compared with measured data and with the results obtained by using the Electromagnetic Surface Patch (ESP) code. From these comparisons, one can conclude that the present method calculates the RCS's of these geometries with good accuracy. Because an irregularly shaped plate is divided into identical rectangular subdomains in the present formulation, the resulting impedance matrix in the moment method is not only symmetrical but also of block Toeplitz nature. This effect is shown to result in a considerable time savings in filling the impedance matrix without sacrificing accuracy.

NASA Langley Research Center  
Hampton, VA 23681-0001  
July 26, 1993

## Appendix

### Description of Floppy Disk Contents

A double-sided/high-density (DS/HD)  $3\frac{1}{2}$ -in. floppy disk containing several data files has been provided for further clarification of this report. These data files contain the experimental data and the computed results used in plotting various figures in the report. The computed and experimental data for a figure are stored in a file having the same name as the figure. For example, the data used to plot figure 3(a) may be found in a file named *fig3a.dat*.

The floppy disk may be read using an IBM PC, PC/XT, or PC/AT with MS-DOS 2.1 or higher and a  $3\frac{1}{2}$ -in. drive. The data on the disk are in a compressed form. To read the data, the file *figure.zip* must be uncompressed first. This is done as shown below. Create a directory called *temp*, and then use the command

```
pkunzip figure.zip c: temp
```

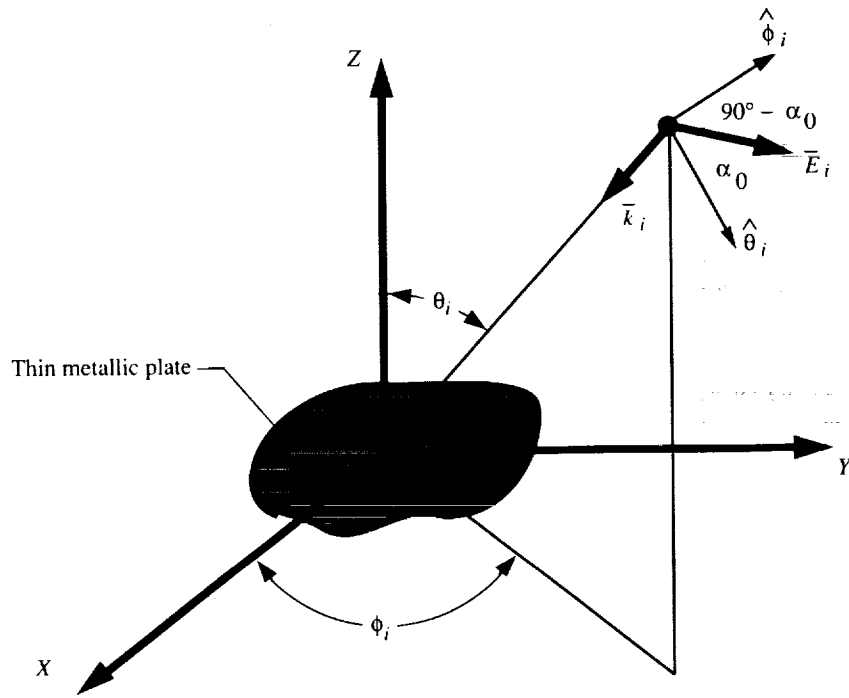
This will write all data files in the *temp* directory.

The reader can obtain a copy of this floppy disk by contacting the authors at the following address:

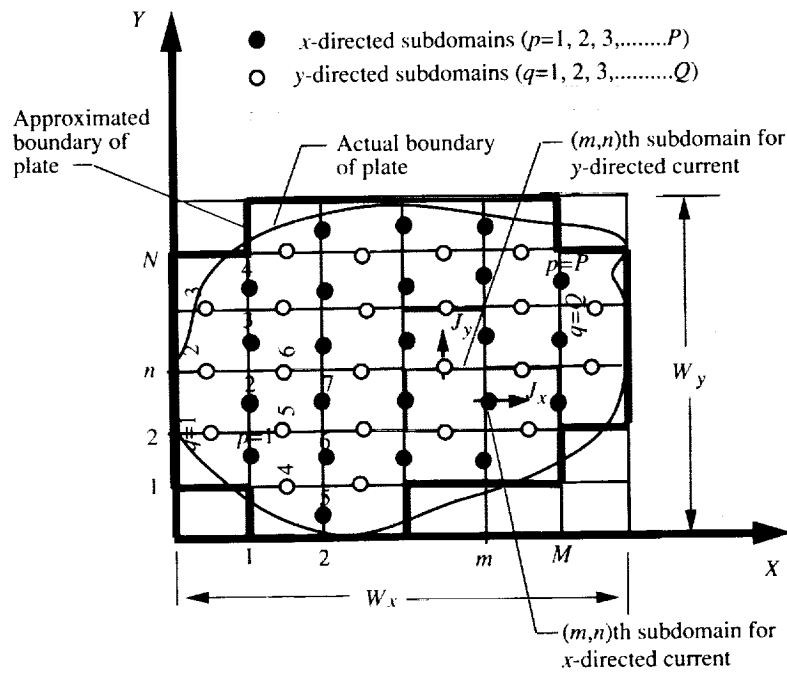
Guidance and Control Division  
Antenna and Microwave Research Branch  
NASA Langley Research Center  
MS 490  
Hampton, VA 23681-0001

## References

1. Newman, Edward H.; and Marhefka, Ronald Joseph: Overview of MM and UTD Methods at the Ohio State University. *Proc. IEEE*, vol. 77, no. 5, May 1989, pp. 700-708.
2. Knepp, Dennis L.; and Goldhirsh, Julius: Numerical Analysis of Electromagnetic Radiation Properties of Smooth Conducting Bodies of Arbitrary Shape. *IEEE Trans. Antennas & Propag.*, vol. AP-20, no. 3, May 1972, pp. 383-388.
3. Singh, J.; and Adams, A. T.: A Nonrectangular Patch Model for Scattering From Surfaces. *IEEE Trans. Antennas & Propag.*, vol. AP-27, July 1979, pp. 531-535.
4. Newman, Edward H.; and Tulyathan, Pravit: A Surface Patch Model for Polygonal Plates. *IEEE Trans. Antennas & Propag.*, vol. AP-30, no. 4, July 1982, pp. 588-593.
5. Pistorius, C. W. I.; and Burnside, W. D.: *New Main Reflector, Subreflector and Dual Chamber Concepts for Compact Range Applications*. NASA CR-181506, 1987.
6. Peters, Timothy J.; and Volakis, John L.: Application of a Conjugate Gradient FFT Method to Scattering From Thin Planar Material Plates. *IEEE Trans. Antennas & Propag.*, vol. 36, no. 4, Apr. 1988, pp. 518-526.
7. Scott, Craig: *The Spectral Domain Method in Electromagnetics*. Artech House, Inc., c.1989.
8. Noble, Ben: *Applied Linear Algebra*. Prentice-Hall, Inc., c.1969.
9. Collin, R. E.; and Zucker, F. J., eds.: *Antenna Theory—Part 1*. McGraw-Hill Book Co., Inc., 1969.
10. Balanis, Constantine A.: *Advanced Engineering Electromagnetics*. John Wiley & Sons, Inc., c.1989.



(a) Plate excited by plane wave.



(b) Plate divided into rectangular subdomains.

Figure 1. Geometry of irregularly shaped, thin, metallic flat plate.

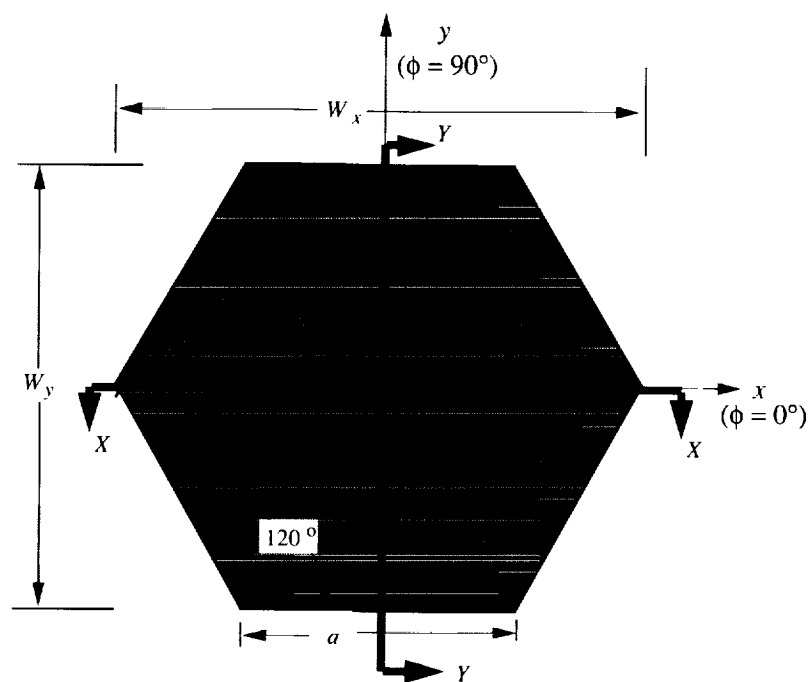
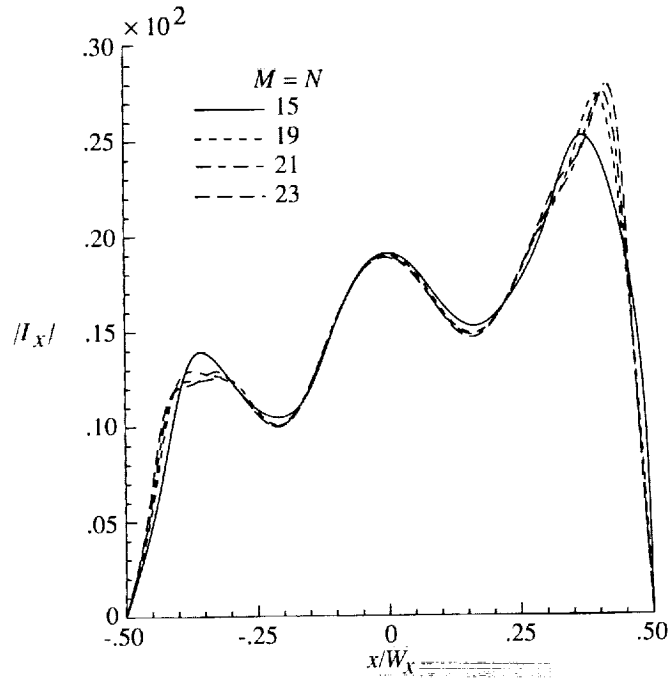
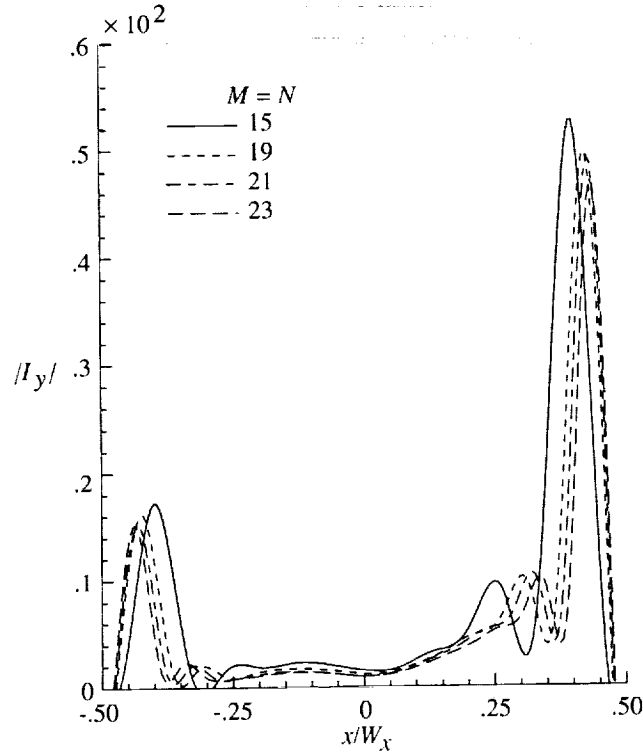


Figure 2. Thin, metallic flat plate of hexagonal shape with  $a = 2.074$  cm.



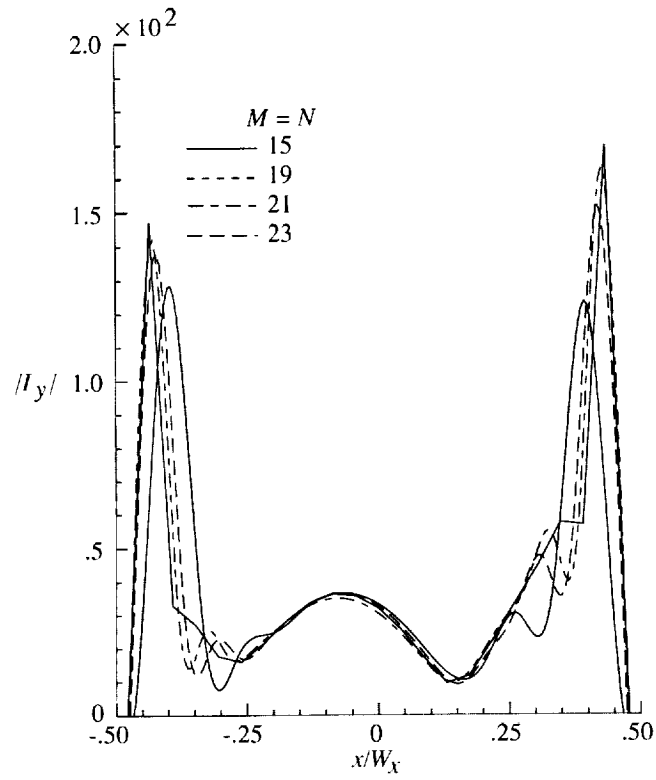
(a)  $x$ -component along  $XX$ -plane with  $H$ -polarized plane wave.



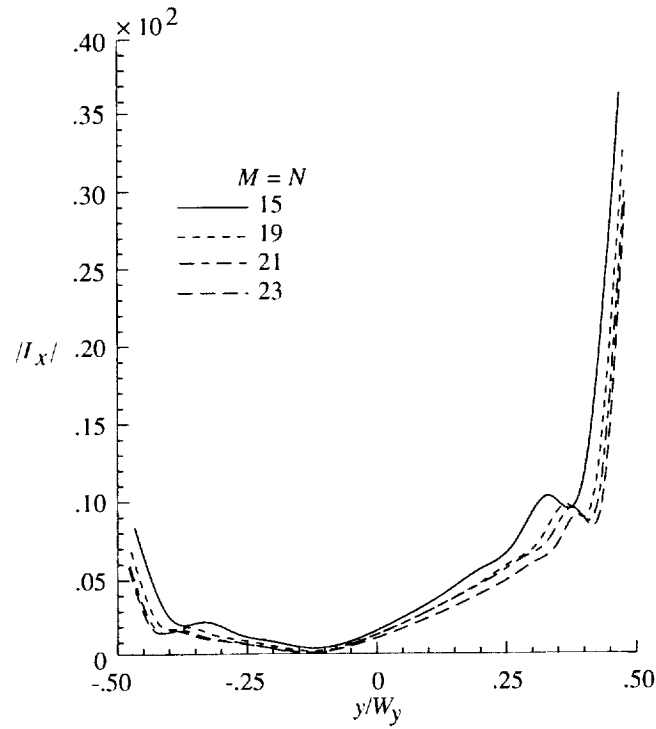
(b)  $y$ -component along  $XX$ -plane with  $H$ -polarized plane wave.

Figure 3. Magnitude of  $x$ - and  $y$ -components of surface-current density along  $XX$ - and  $YY$ -planes on hexagonal plate (shown in fig. 2) excited by  $H$ - and  $E$ -polarized plane waves with angle of incidence ( $\theta_i = 80^\circ, \phi_i = 0^\circ$ ) for  $M = N = 15, 19, 21$ , and  $23$ .



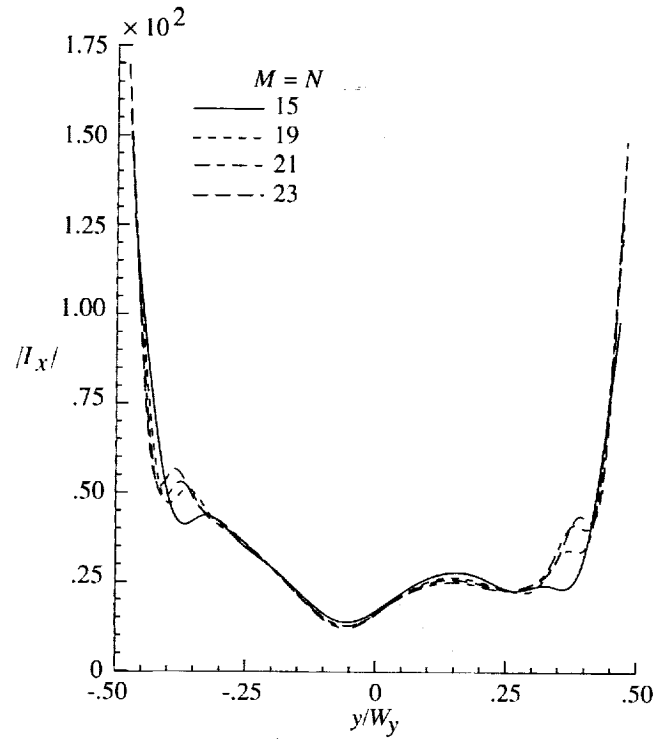


(c)  $y$ -component along  $XX$ -plane with  $E$ -polarized plane wave.

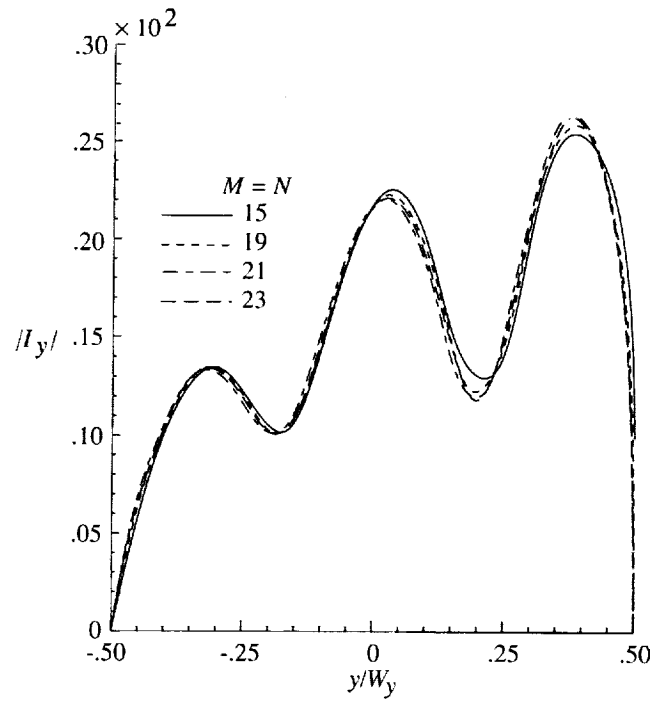


(d)  $x$ -component along  $YY$ -plane with  $H$ -polarized plane wave.

Figure 3. Continued.

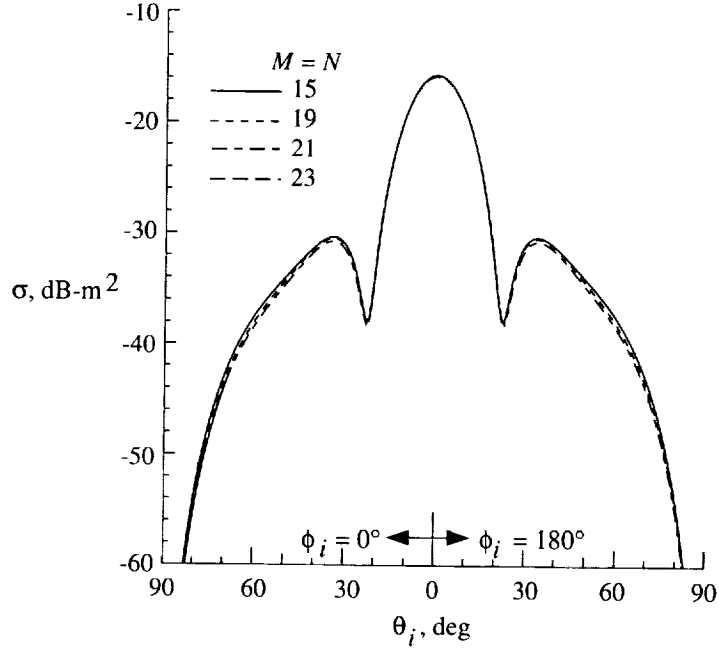


(e)  $x$ -component along  $YY$ -plane with  $E$ -polarized plane wave.

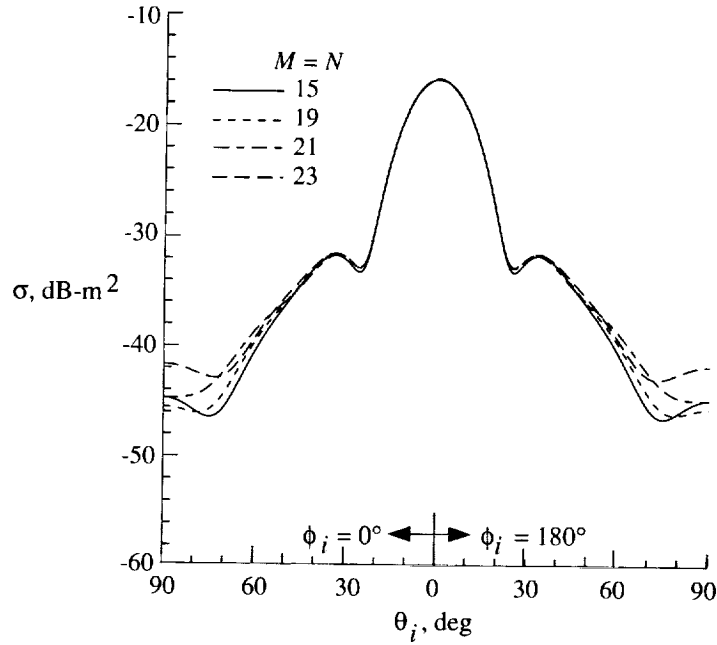


(f)  $y$ -component along  $YY$ -plane with  $H$ -polarized plane wave.

Figure 3. Concluded.

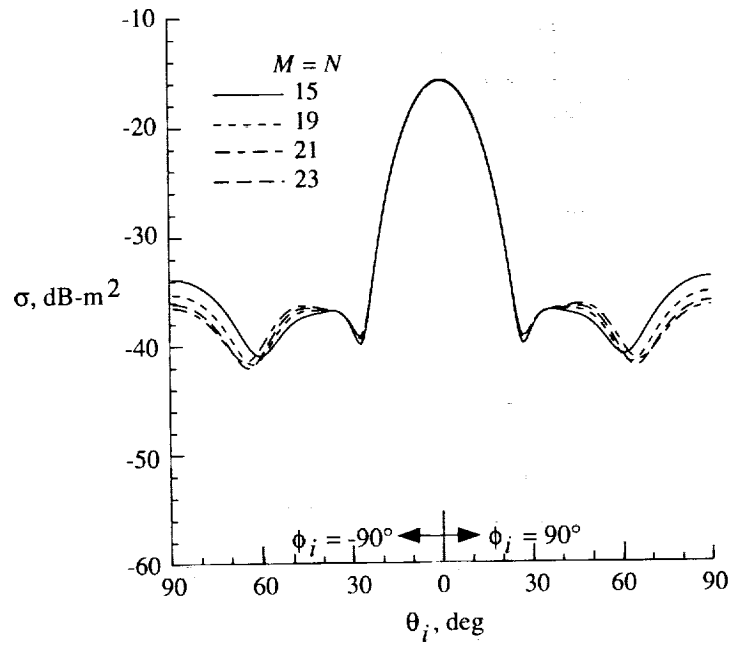


(a)  $H$ -polarized plane wave ( $\alpha_0 = 0^\circ$ ) at  $\phi_i = 0^\circ$  and  $180^\circ$ .

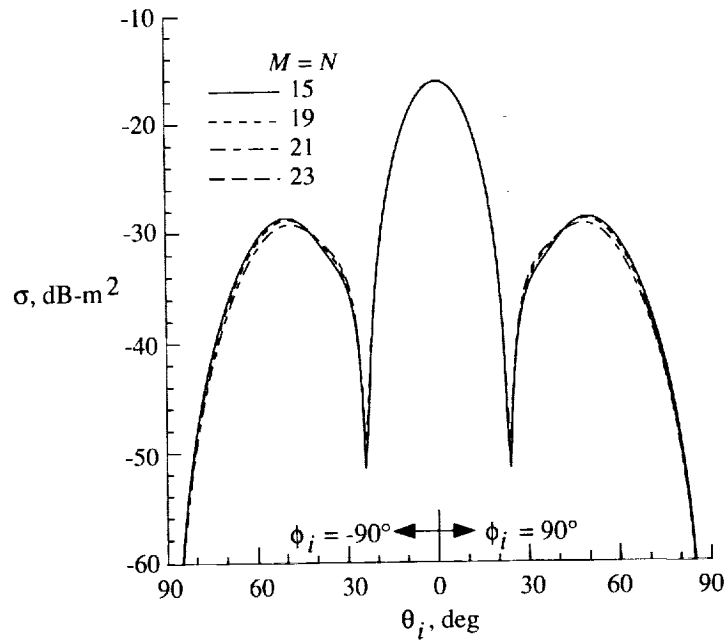


(b)  $E$ -polarized plane wave ( $\alpha_0 = 90^\circ$ ) at  $\phi_i = 0^\circ$  and  $180^\circ$ .

Figure 4. Monostatic RCS of hexagonal plate (shown in fig. 2) excited by  $H$ - and  $E$ -polarized plane waves ( $\alpha_0 = 0^\circ$  and  $90^\circ$ , respectively) as a function of  $\theta_i$  for  $f = 11.811$  GHz with  $M = N = 15, 19, 21$ , and  $23$ .



(c) *E*-polarized plane wave ( $\alpha_0 = 90^\circ$ ) at  $\phi_i = -90^\circ$  and  $90^\circ$ .



(d) *H*-polarized plane wave ( $\alpha_0 = 0^\circ$ ) at  $\phi_i = -90^\circ$  and  $90^\circ$ .

Figure 4. Concluded.

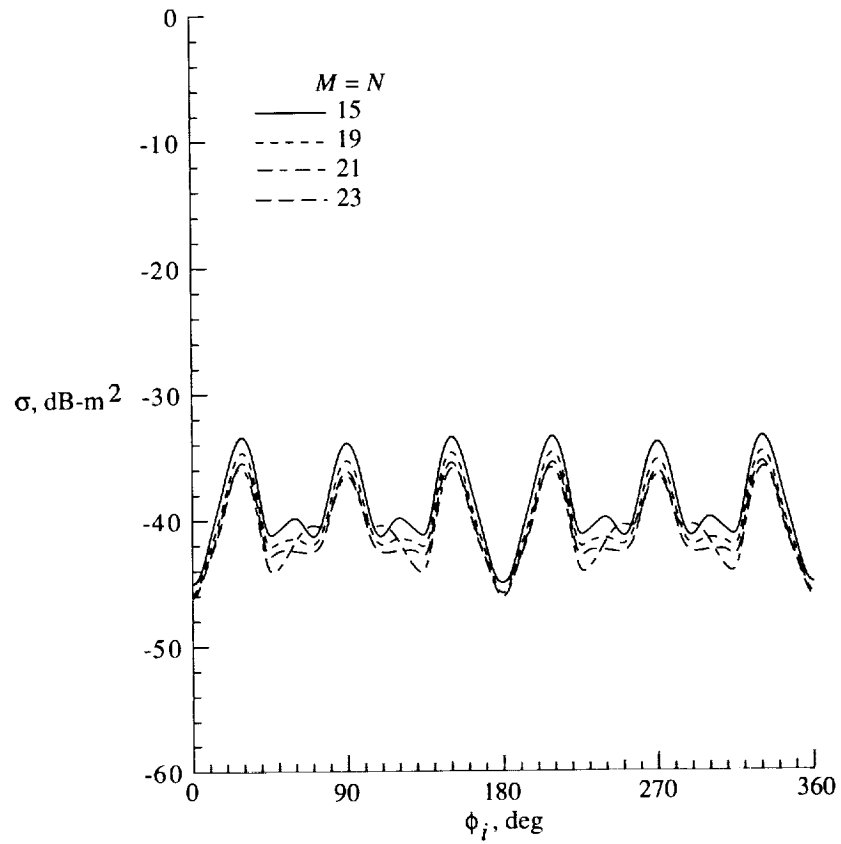
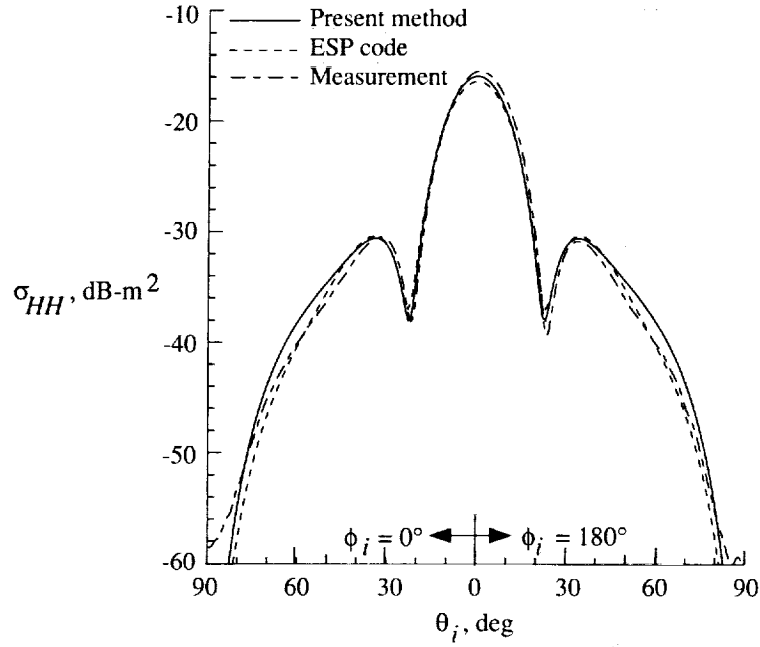
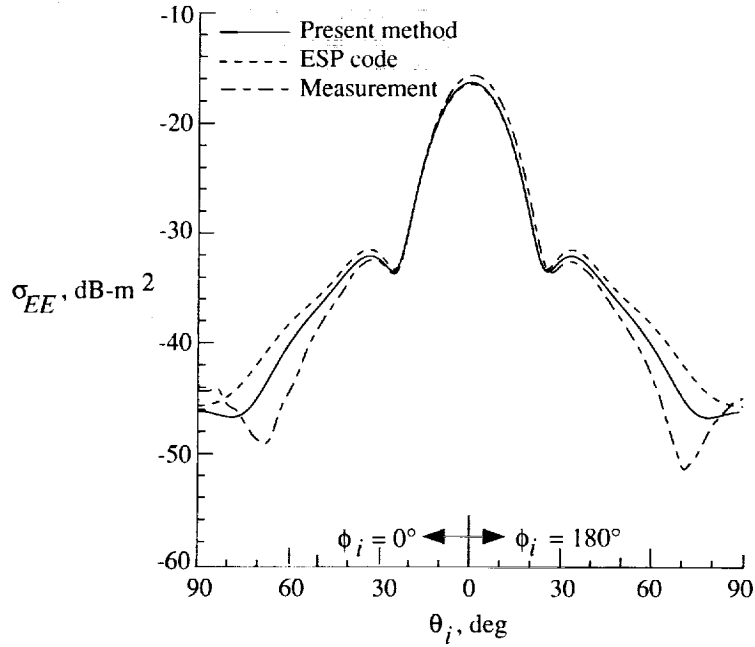


Figure 5. Monostatic RCS of hexagonal plate (shown in fig. 2) excited by  $E$ -polarized plane wave ( $\alpha_0 = 90^\circ$ ) as a function of  $\phi_i$  for  $f = 11.811$  GHz with  $M = N = 15, 19, 21$ , and  $23$  and  $\theta_i = 90^\circ$  (grazing incidence).

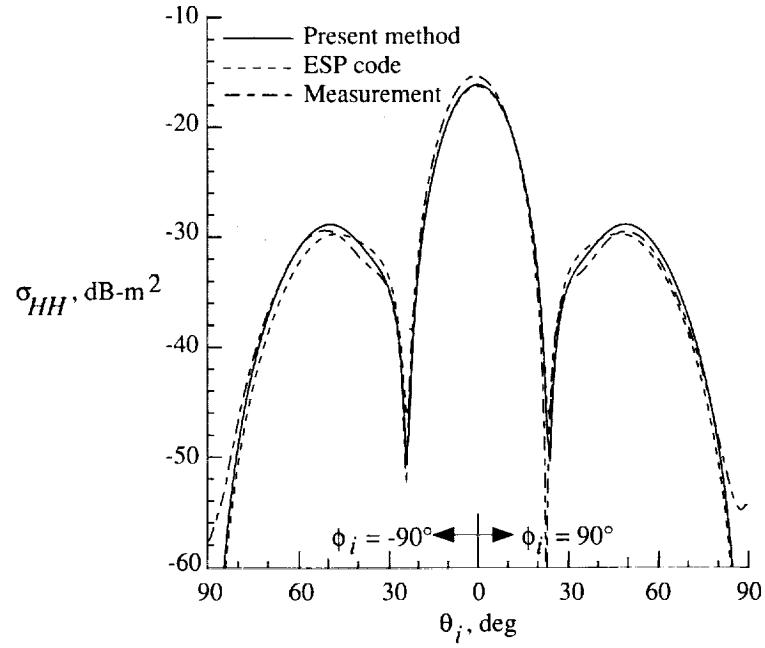


(a)  $H$ -polarized plane wave ( $\alpha_0 = 0^\circ$ ) at  $\phi_i = 0^\circ$  and  $180^\circ$ .

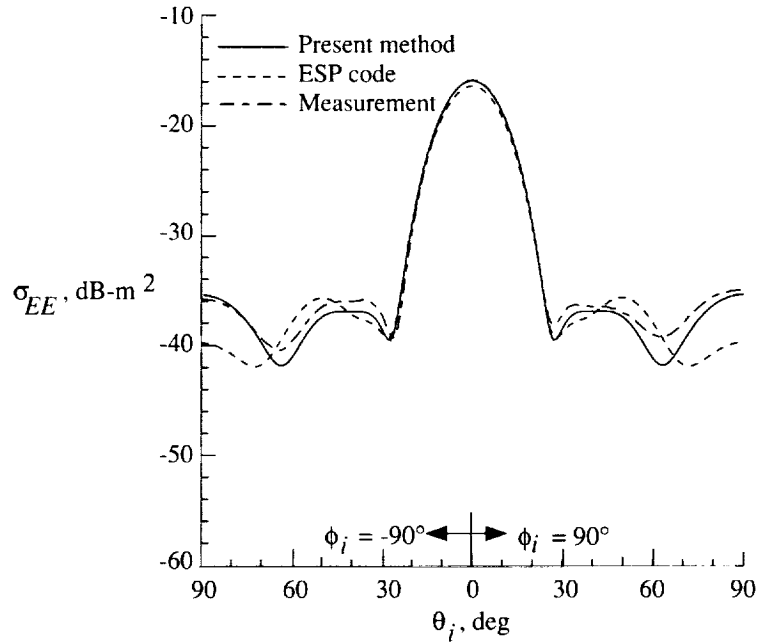


(b)  $E$ -polarized plane wave ( $\alpha_0 = 90^\circ$ ) at  $\phi_i = 0^\circ$  and  $180^\circ$ .

Figure 6. Monostatic RCS of hexagonal plate (shown in fig. 2) excited by  $H$ - and  $E$ -polarized plane waves ( $\alpha_0 = 0^\circ$  and  $90^\circ$ , respectively) as a function of  $\theta_i$  for  $f = 11.811$  GHz with  $M = N = 19$ .



(c)  $H$ -polarized plane wave ( $\alpha_0 = 0^\circ$ ) at  $\phi_i = -90^\circ$  and  $90^\circ$ .



(d)  $E$ -polarized plane wave ( $\alpha_0 = 90^\circ$ ) at  $\phi_i = -90^\circ$  and  $90^\circ$ .

Figure 6. Concluded.

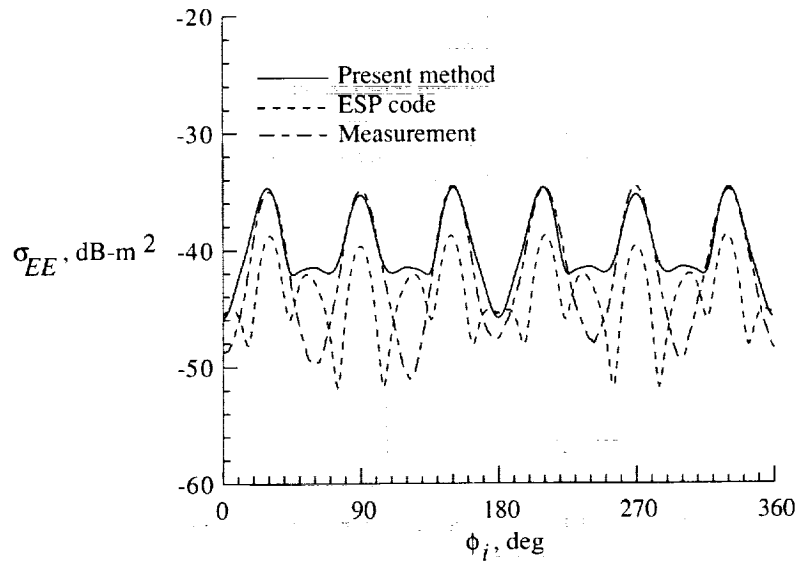


Figure 7. Monostatic RCS of hexagonal plate (shown in fig. 2) excited by  $E$ -polarized plane wave ( $\alpha_0 = 90^\circ$ ) as a function of  $\phi_i$  for  $f = 11.811$  GHz with  $M = N = 19$  and  $\theta_i = 90^\circ$  (grazing incidence).

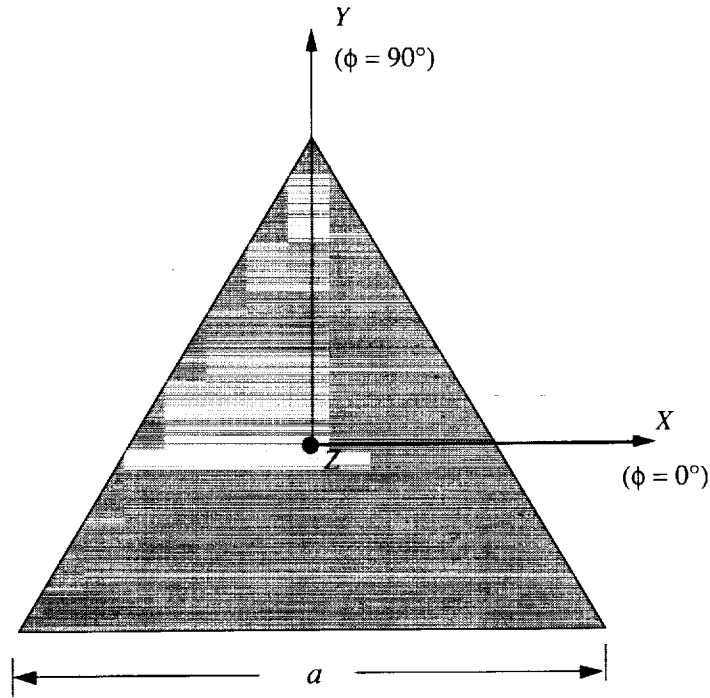
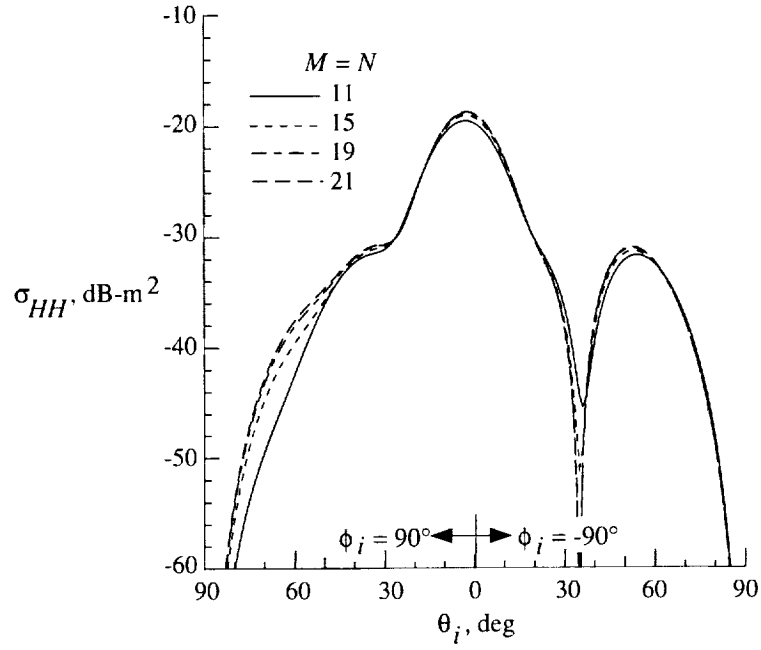
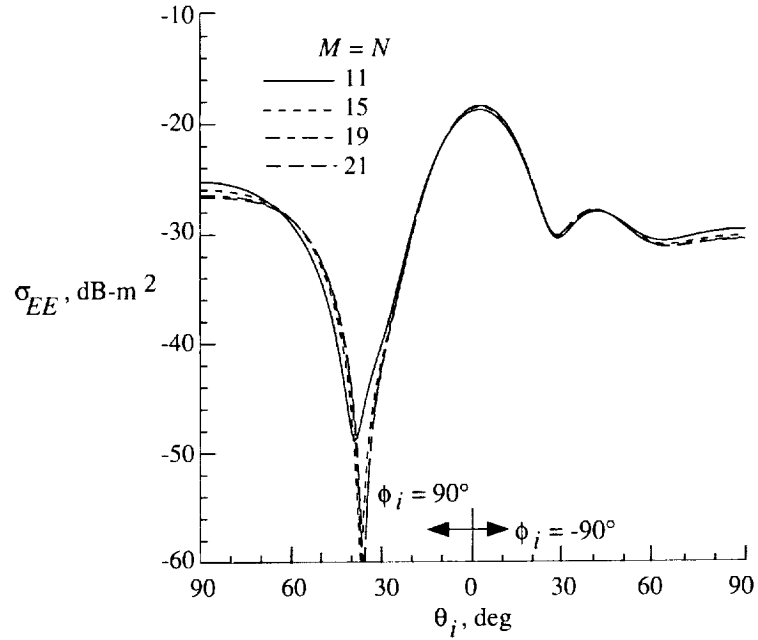


Figure 8. Equilateral triangular, thin, metallic flat plate with  $a = 5.08$  cm lying in  $XY$ -plane.



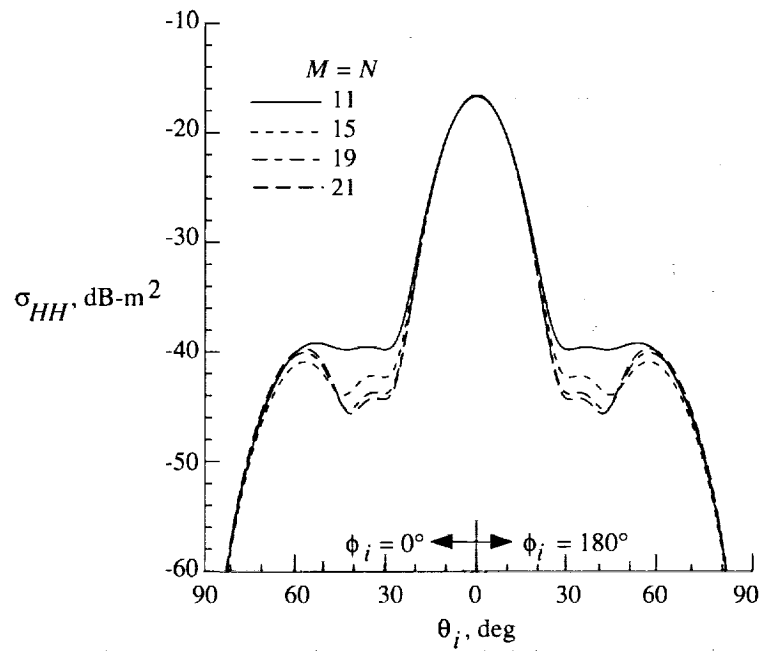


(a)  $H$ -polarized plane wave ( $\alpha_0 = 0^\circ$ ) at  $\phi_i = 90^\circ$  and  $-90^\circ$ .

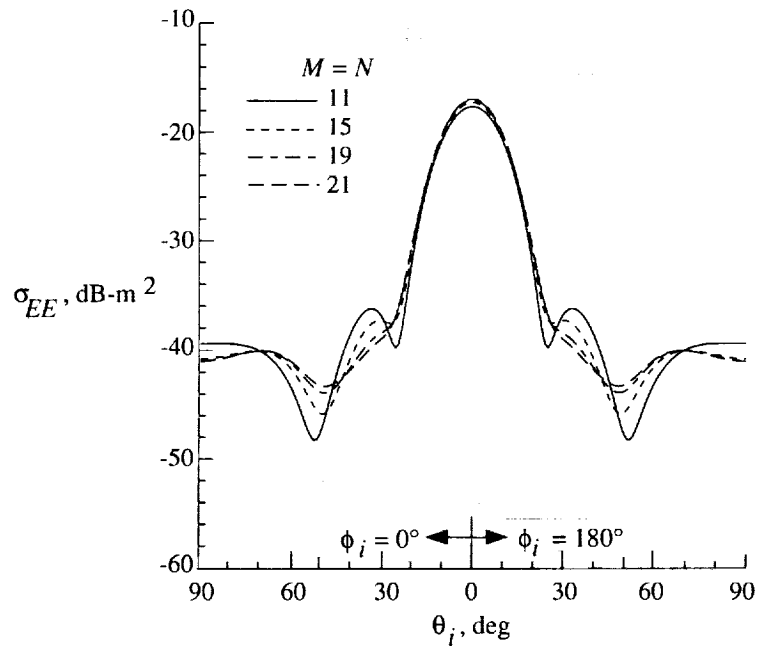


(b)  $E$ -polarized plane wave ( $\alpha_0 = 90^\circ$ ) at  $\phi_i = 90^\circ$  and  $-90^\circ$ .

Figure 9. Monostatic RCS of equilateral triangular plate (shown in fig. 8) excited by  $H$ - and  $E$ -polarized plane waves ( $\alpha_0 = 0^\circ$  and  $90^\circ$ , respectively) as a function of  $\theta_i$  for  $f = 11.811$  GHz with  $M = N = 11, 15, 19$ , and  $21$ .

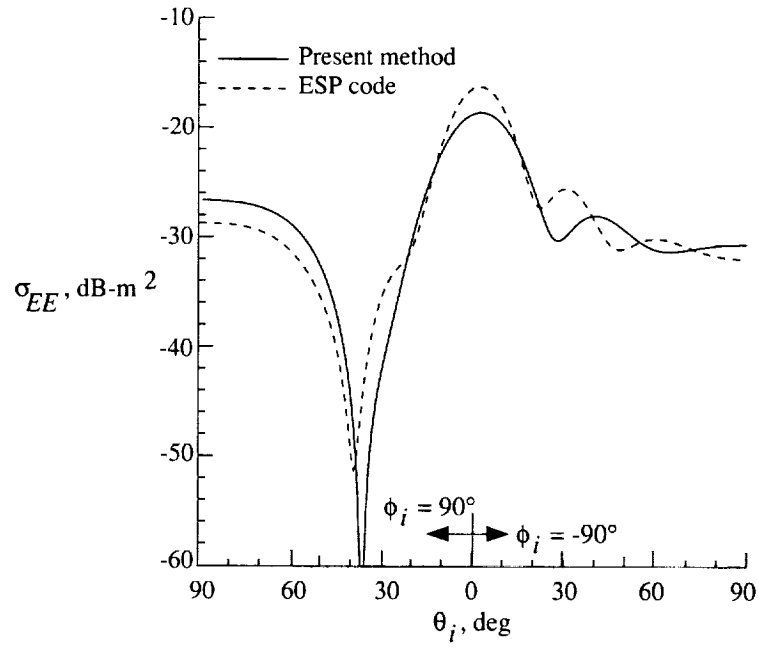


(c)  $H$ -polarized plane wave ( $\alpha_0 = 0^\circ$ ) at  $\phi_i = 0^\circ$  and  $180^\circ$ .

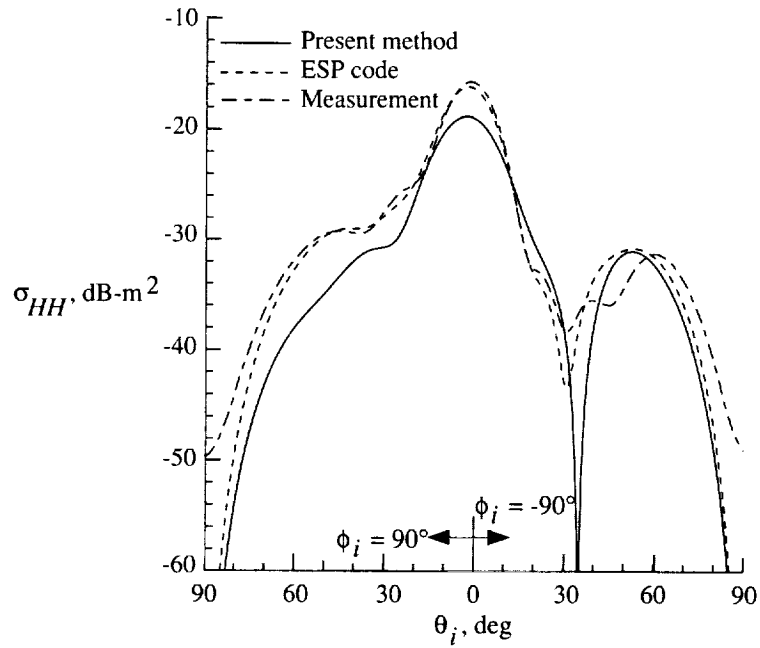


(d)  $E$ -polarized plane wave ( $\alpha_0 = 90^\circ$ ) at  $\phi_i = 0^\circ$  and  $180^\circ$ .

Figure 9. Concluded.

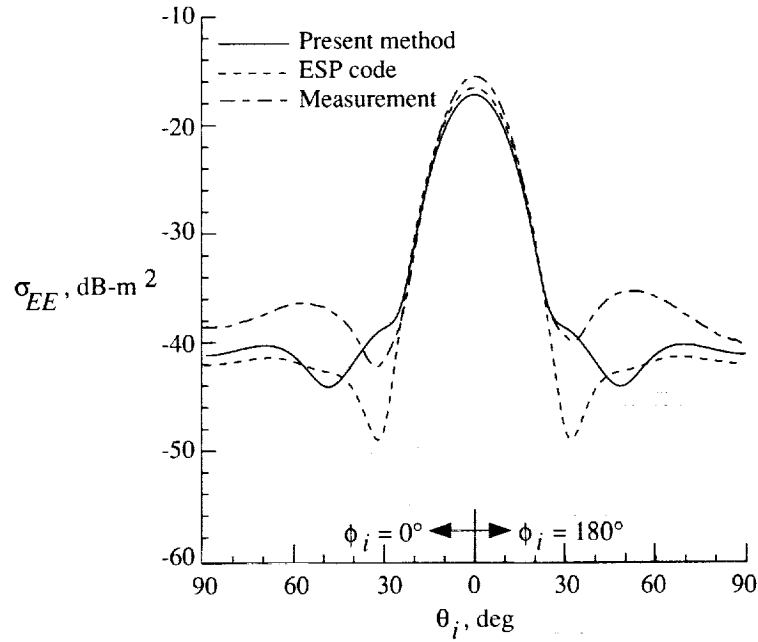


(a)  $E$ -polarized plane wave ( $\alpha_0 = 90^\circ$ ) at  $\phi_i = 90^\circ$  and  $-90^\circ$ .

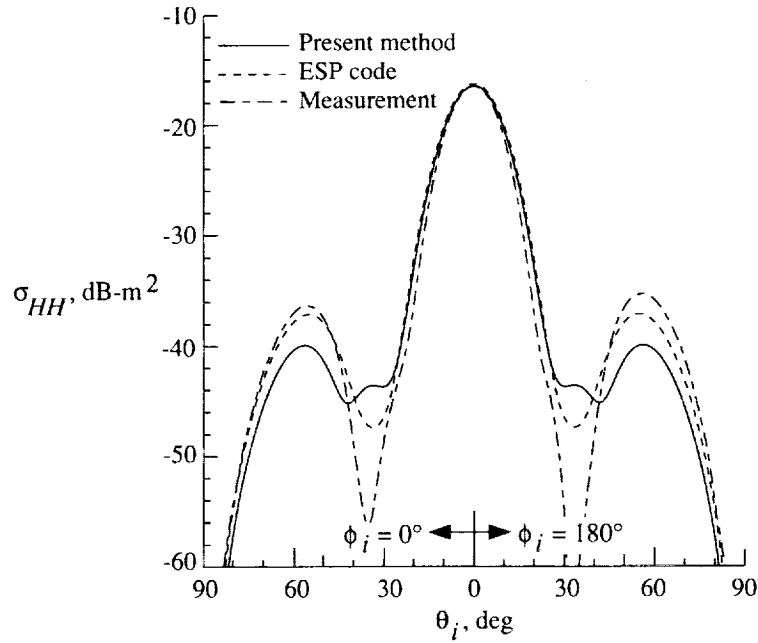


(b)  $H$ -polarized plane wave ( $\alpha_0 = 0^\circ$ ) at  $\phi_i = 90^\circ$  and  $-90^\circ$ .

Figure 10. Monostatic RCS of equilateral triangular plate (shown in fig. 8) excited by  $H$ - and  $E$ -polarized plane waves ( $\alpha_0 = 0^\circ$  and  $90^\circ$ , respectively) as a function of  $\theta_i$  for  $f = 11.811$  GHz and  $M = N = 19$ .



(c) *E*-polarized plane wave ( $\alpha_0 = 90^\circ$ ) at  $\phi_i = 0^\circ$  and  $180^\circ$ .



(d) *H*-polarized plane wave ( $\alpha_0 = 0^\circ$ ) at  $\phi_i = 0^\circ$  and  $180^\circ$ .

Figure 10. Concluded.

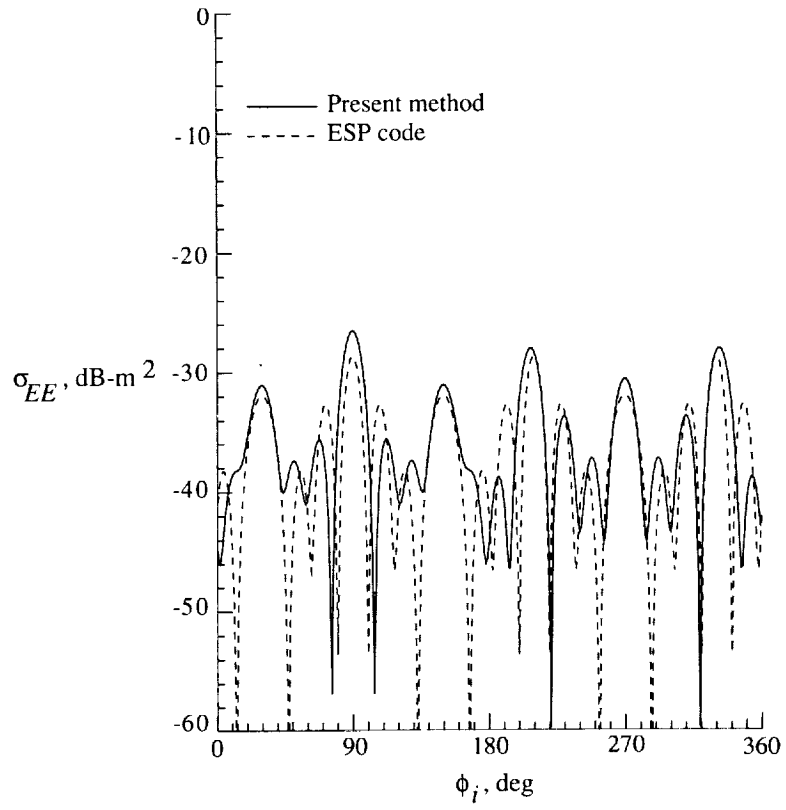
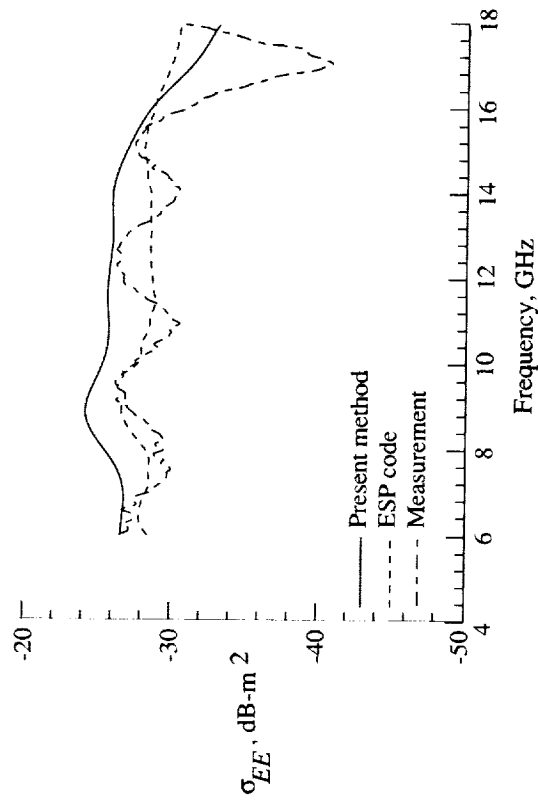
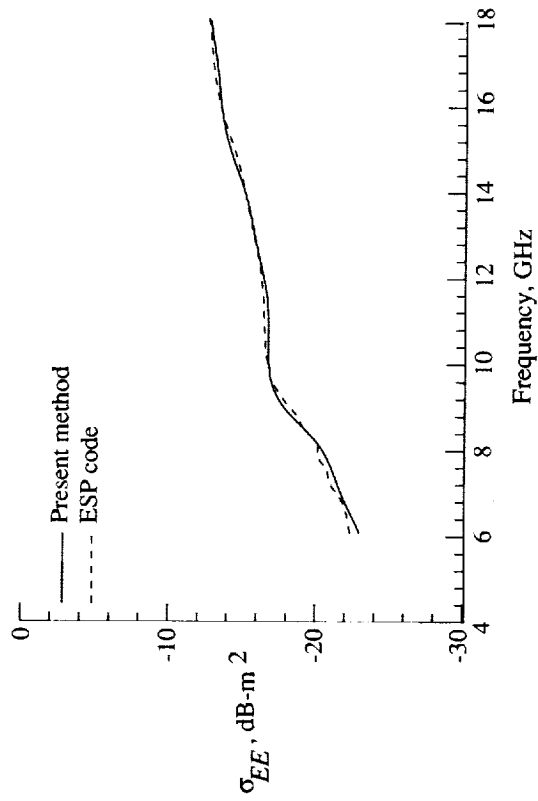


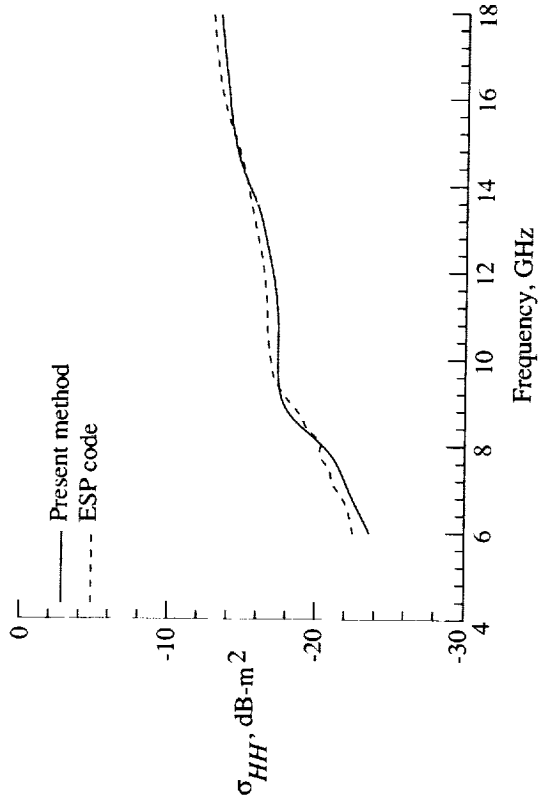
Figure 11. Monostatic RCS of equilateral triangular plate (shown in fig. 8) excited by  $E$ -polarized plane wave ( $\alpha_0 = 90^\circ$ ) as a function of  $\phi_i$  for  $f = 11.811$  GHz with  $M = N = 19$  and  $\theta_i = 90^\circ$  (grazing incidence).



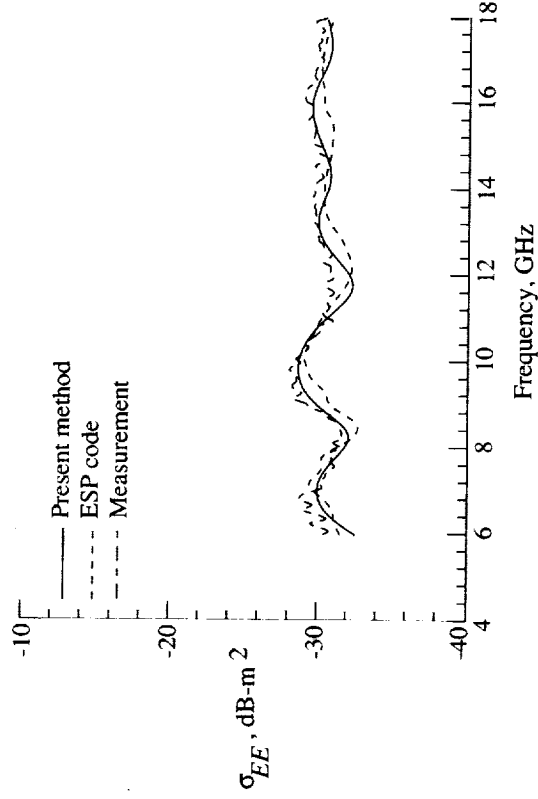
(a)  $E$ -polarized plane wave ( $\alpha_0 = 90^\circ$ ) at  $\theta_i = 90^\circ$ ,  $\phi_i = 90^\circ$  with grazing incidence at tip.



(c)  $E$ -polarized plane wave ( $\alpha_0 = 90^\circ$ ) at  $\theta_i = 0^\circ$ ,  $\phi_i = 90^\circ$  with normal incidence.



(b)  $H$ -polarized plane wave ( $\alpha_0 = 0^\circ$ ) at  $\theta_i = 0^\circ$ ,  $\phi_i = 90^\circ$  with normal incidence.



(d)  $E$ -polarized plane wave ( $\alpha_0 = 90^\circ$ ) at  $\theta_i = 90^\circ$ ,  $\phi_i = -90^\circ$  with grazing incidence at edge.

Figure 12. Monostatic RCS of equilateral triangular plate (shown in fig. 8) excited by  $H$ - and  $E$ -polarized plane waves ( $\alpha_0 = 0^\circ$  and  $90^\circ$ , respectively) at angles of incidence as a function of frequency for  $M = N = 19$ .

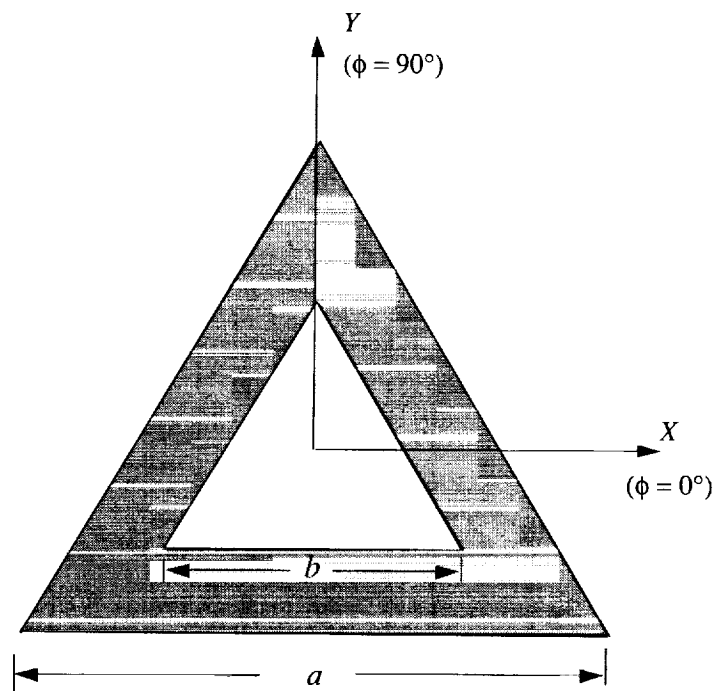
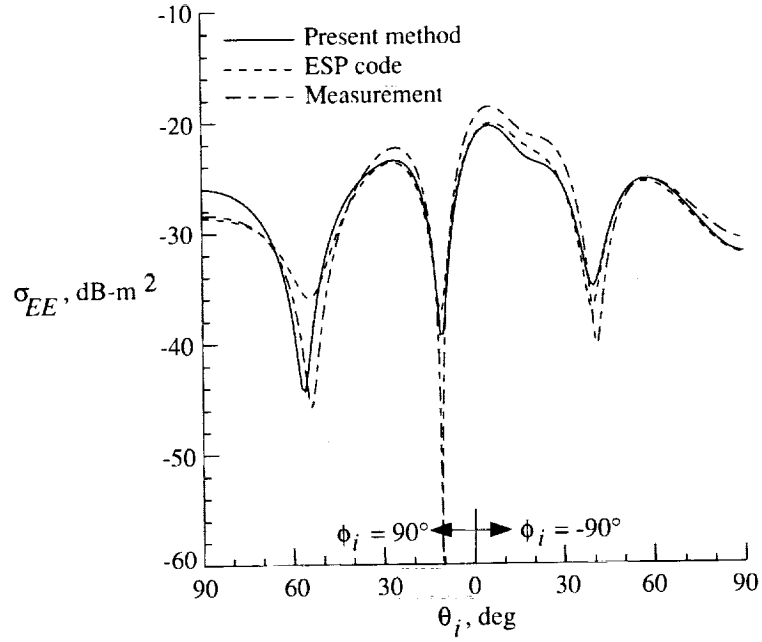
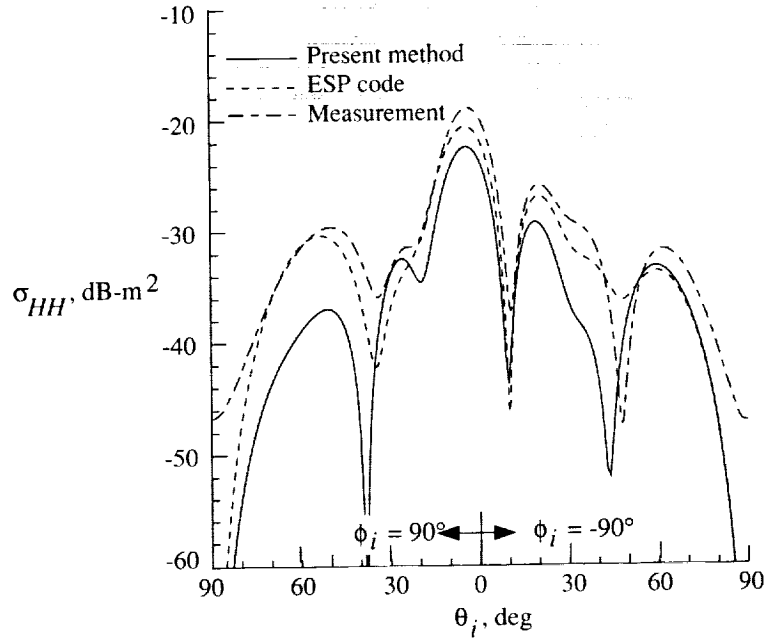


Figure 13. Equilateral, triangular, thin, metallic flat plate with concentric, equilateral triangular hole with  $a = 5.08$  cm and  $b = 2.54$  cm.



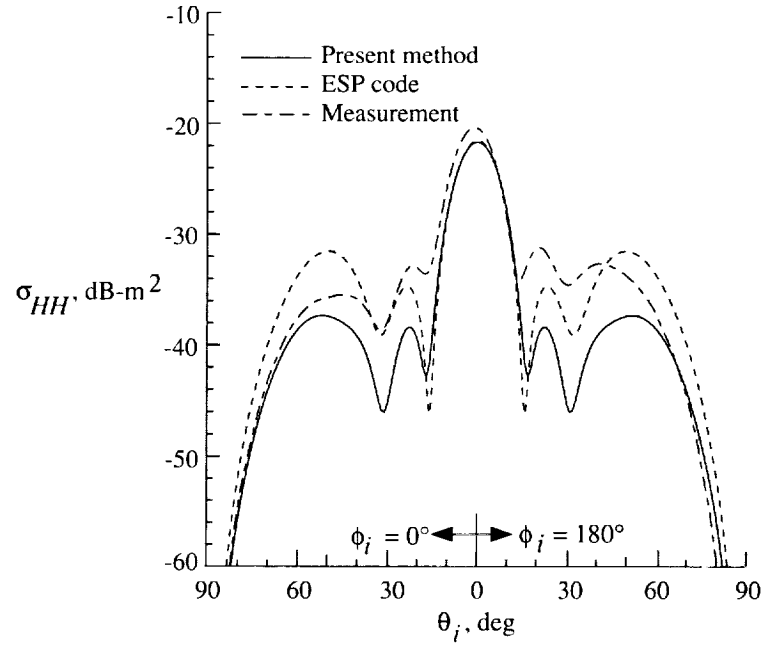
(a)  $E$ -polarized plane wave ( $\alpha_0 = 90^\circ$ ) at  $\phi_i = 90^\circ$  and  $-90^\circ$ .



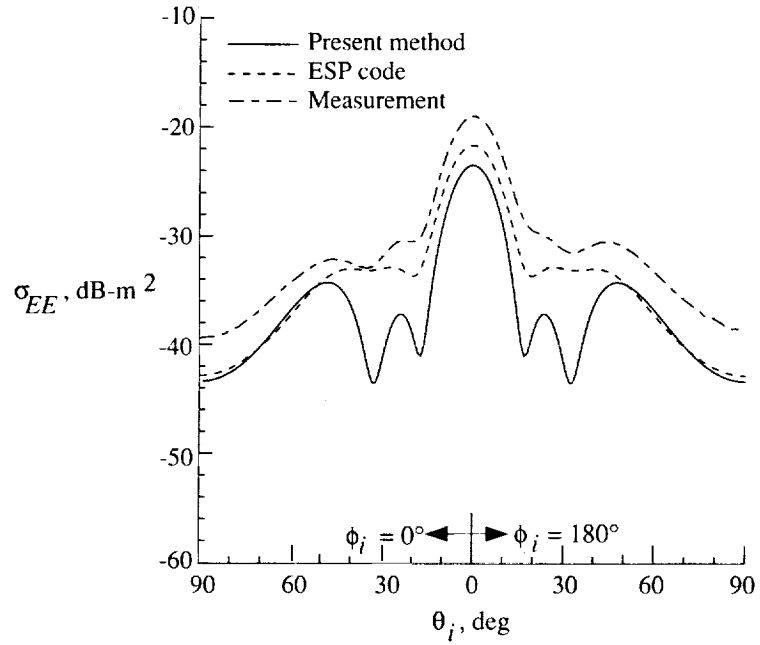
(b)  $H$ -polarized plane wave ( $\alpha_0 = 0^\circ$ ) at  $\phi_i = 90^\circ$  and  $-90^\circ$ .

Figure 14. Monostatic RCS of equilateral triangular plate (shown in fig. 13) excited by  $H$ - and  $E$ -polarized plane waves ( $\alpha_0 = 0^\circ$  and  $90^\circ$ , respectively) as a function of  $\theta_i$  for  $f = 11.811$  GHz with  $M = N = 19$ .





(c)  $H$ -polarized plane wave ( $\alpha_0 = 0^\circ$ ) at  $\phi_i = 0^\circ$  and  $180^\circ$ .



(d)  $E$ -polarized plane wave ( $\alpha_0 = 90^\circ$ ) at  $\phi_i = 0^\circ$  and  $180^\circ$ .

Figure 14. Concluded.

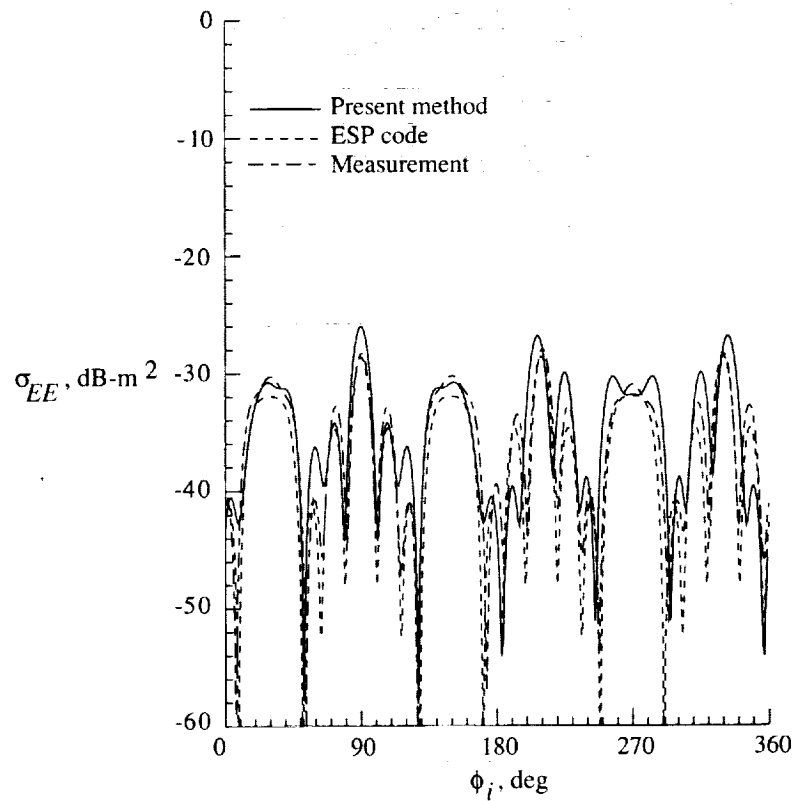
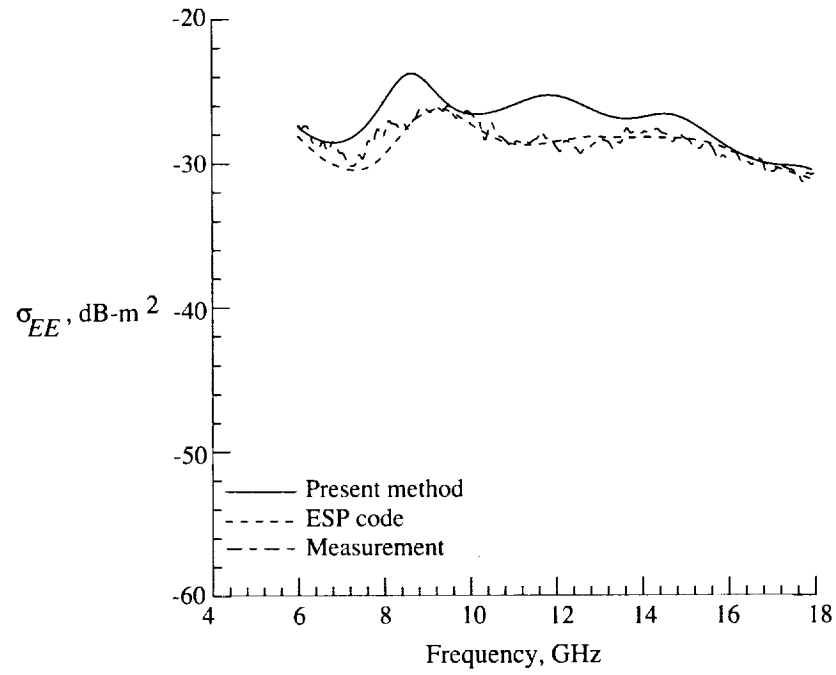
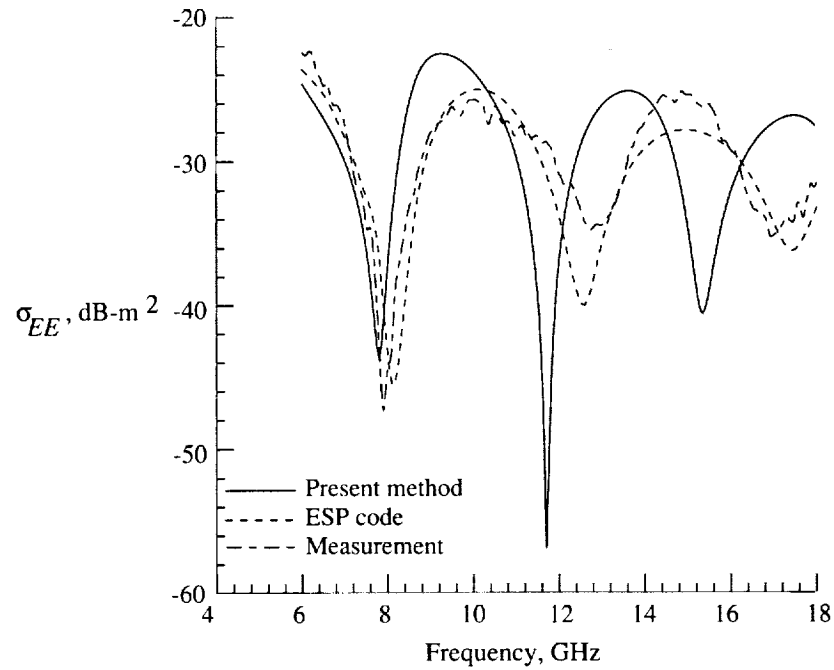


Figure 15. Monostatic RCS of equilateral triangular plate with concentric, equilateral triangular hole (shown in fig. 13) excited by  $E$ -polarized plane wave ( $\alpha_0 = 90^\circ$ ) as a function of  $\phi_i$  for  $f = 11.811$  GHz with  $M = N = 19$  and  $\theta_i = 90^\circ$  (grazing incidence).



(a)  $\theta_i = 90^\circ$ ,  $\phi_i = 90^\circ$  with grazing incidence at tip.



(b)  $\theta_i = 90^\circ$ ,  $\phi_i = -90^\circ$  with grazing incidence at edge.

Figure 16. Monostatic RCS of equilateral triangular plate with concentric, equilateral triangular hole (shown in fig. 13) excited by  $E$ -polarized plane waves ( $\alpha_0 = 90^\circ$ ) at angles of incidence as a function of frequency for  $M = N = 19$ .

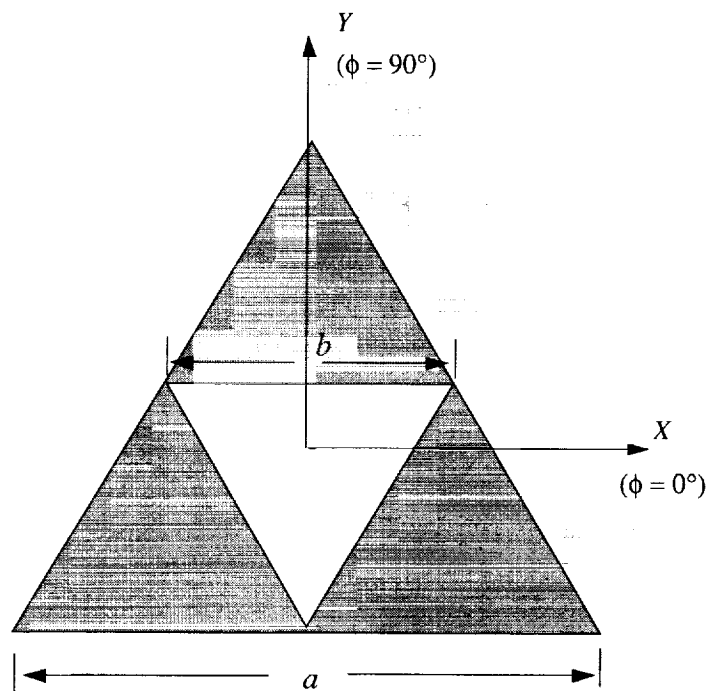
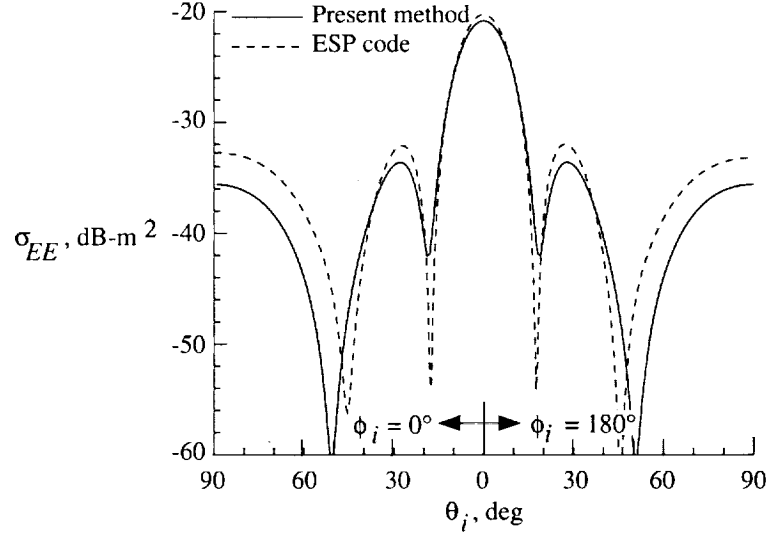
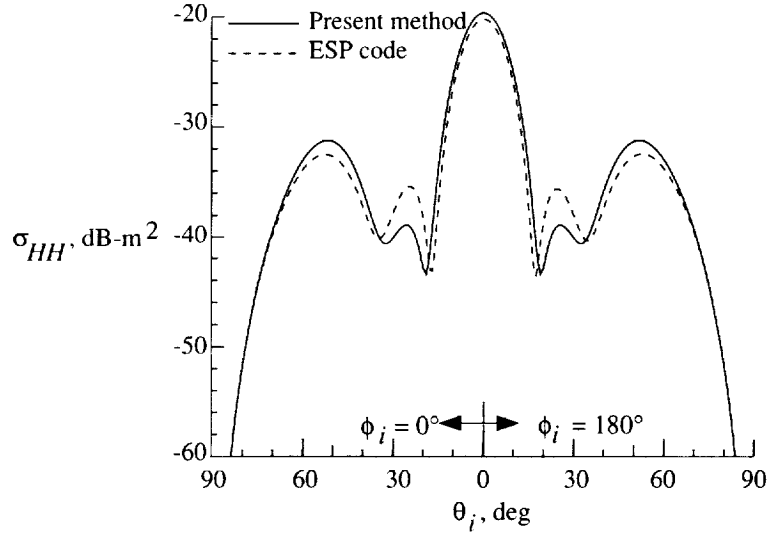


Figure 17. Equilateral, triangular, thin, metallic flat plate with inverted equilateral triangular hole with  $a = 5.08$  cm and  $b = 2.54$  cm.

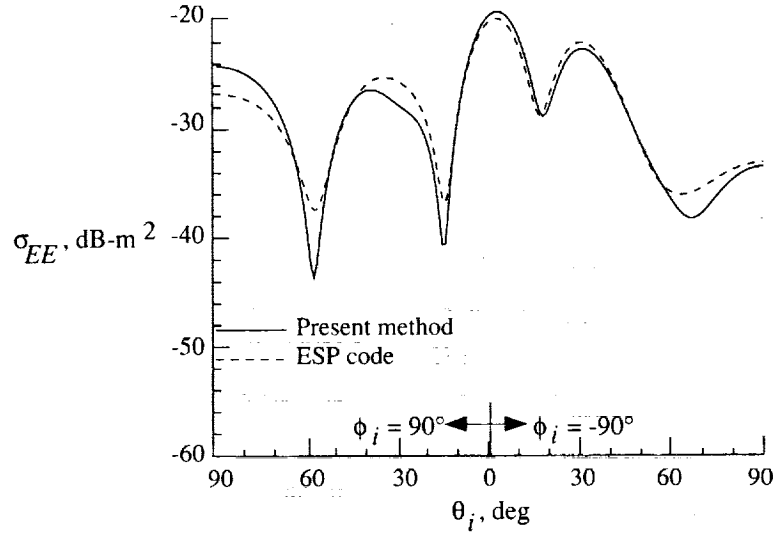


(a)  $E$ -polarized plane wave ( $\alpha_0 = 90^\circ$ ) at  $\phi_i = 0^\circ$  and  $180^\circ$ .

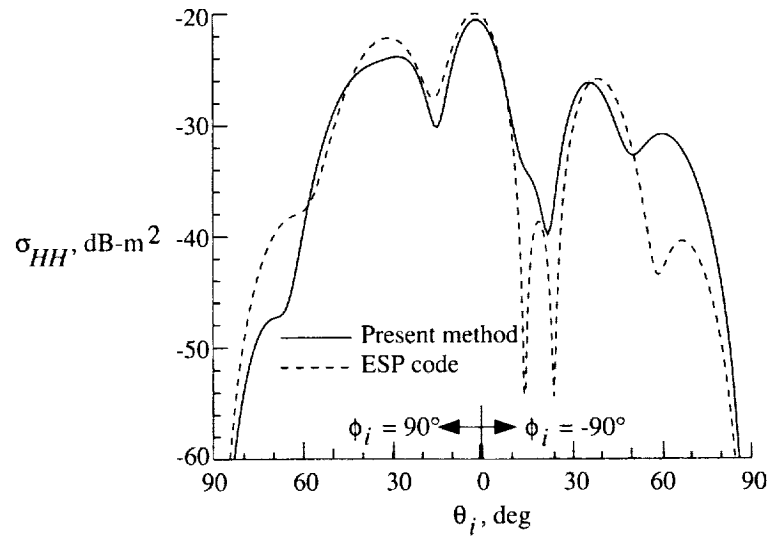


(b)  $H$ -polarized plane wave ( $\alpha_0 = 0^\circ$ ) at  $\phi_i = 0^\circ$  and  $180^\circ$ .

Figure 18. Monostatic RCS of equilateral triangular plate with inverted, equilateral triangular hole (shown in fig. 17) excited by  $H$ - and  $E$ -polarized plane waves ( $\alpha_0 = 0^\circ$  and  $90^\circ$ , respectively) as a function of  $\theta_i$  for  $f = 11.811$  GHz with  $M = N = 19$ .



(c) *E*-polarized plane wave ( $\alpha_0 = 90^\circ$ ) at  $\phi_i = 90^\circ$  and  $-90^\circ$ .



(d) *H*-polarized plane wave ( $\alpha_0 = 0^\circ$ ) at  $\phi_i = 90^\circ$  and  $-90^\circ$ .

Figure 18. Concluded.

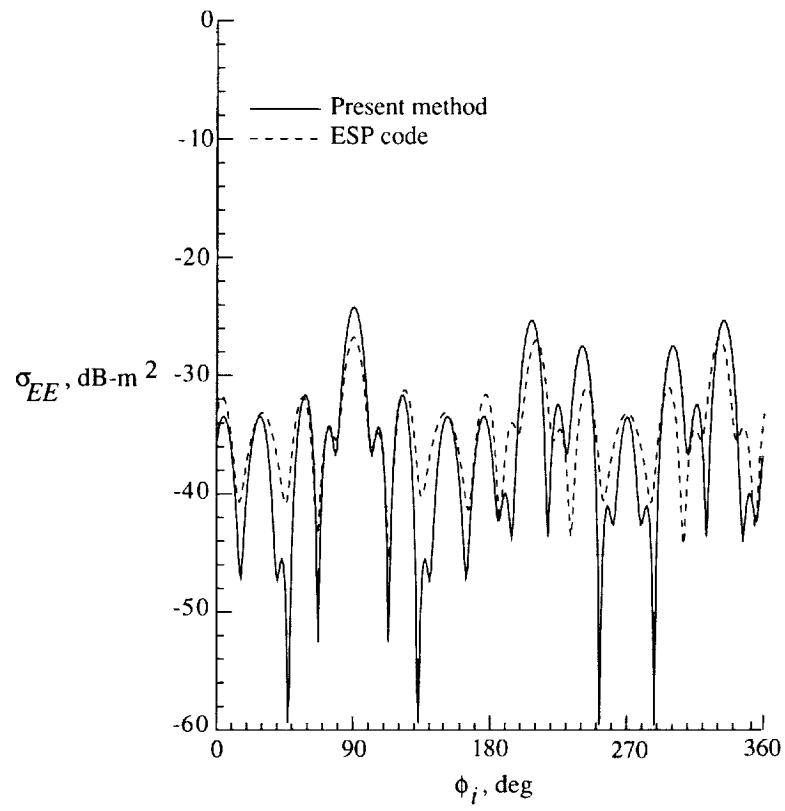
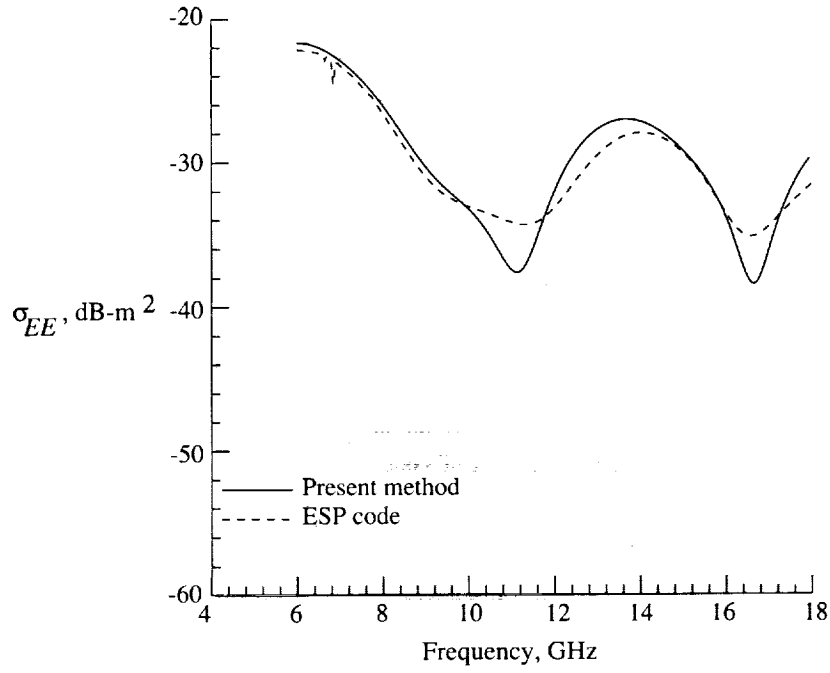
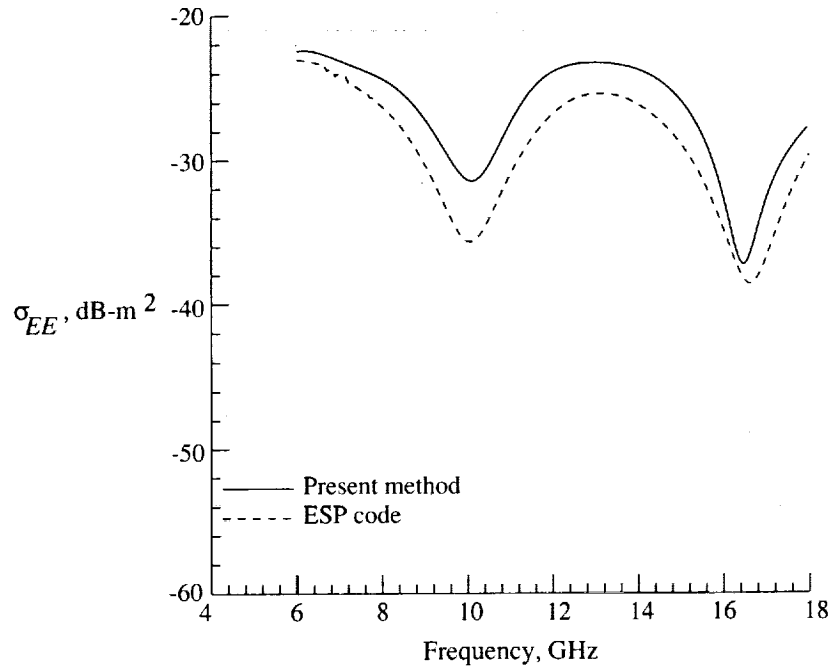


Figure 19. Monostatic RCS of equilateral triangular plate with inverted equilateral triangular hole (shown in fig. 17) excited by  $E$ -polarized plane wave ( $\alpha_0 = 90^\circ$ ) as a function of  $\phi_i$  for  $f = 11.811$  GHz with  $M = N = 19$  and  $\theta_i = 90^\circ$  (grazing incidence).



(a)  $\theta_i = 90^\circ$ ,  $\phi_i = 90^\circ$ .



(b)  $\theta_i = 90^\circ$ ,  $\phi_i = -90^\circ$ .

Figure 20. Monostatic RCS of equilateral triangular plate with inverted, equilateral triangular hole (shown in fig. 17) excited by  $E$ -polarized plane wave ( $\alpha_0 = 90^\circ$ ) at angles of incidence as a function of frequency for  $M = N = 19$ .



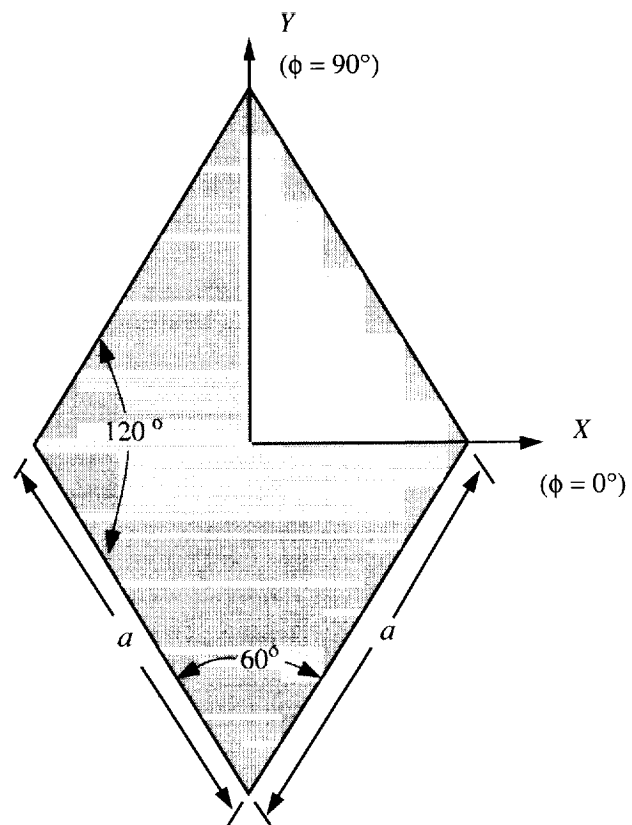
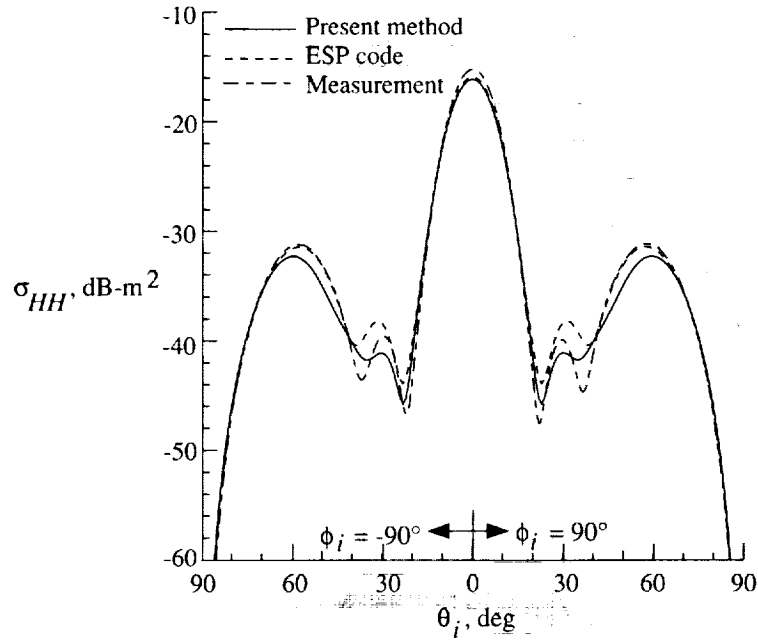
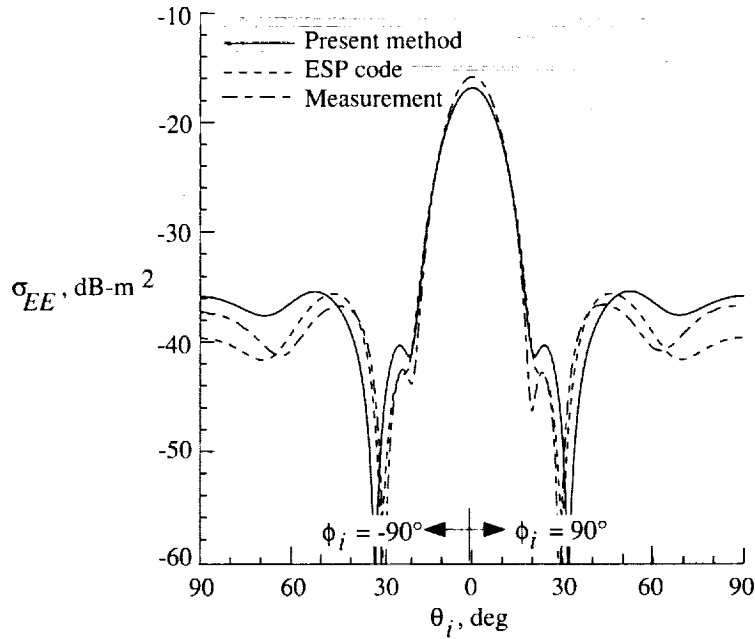


Figure 21. Thin, metallic, diamond-shaped flat plate with  $a = 3.592$  cm.

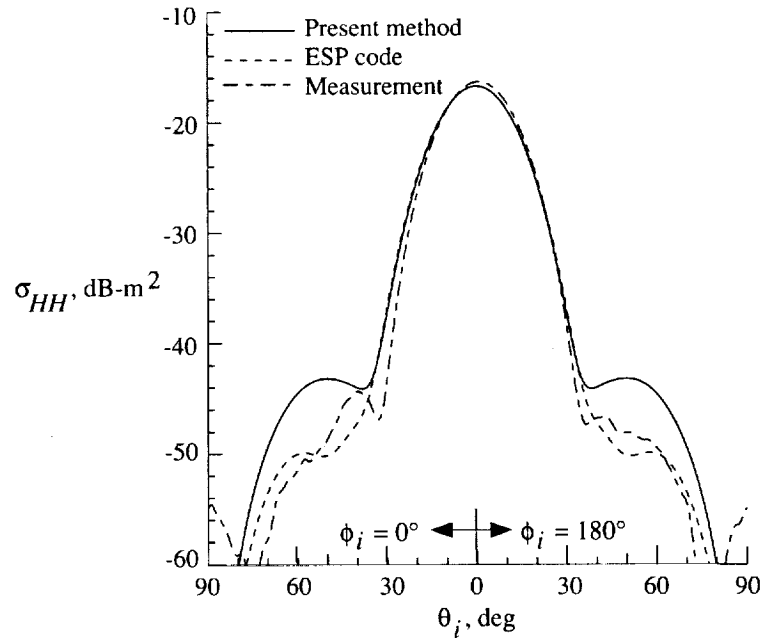


(a)  $H$ -polarized plane wave ( $\alpha_0 = 0^\circ$ ) at  $\phi_i = -90^\circ$  and  $90^\circ$ .

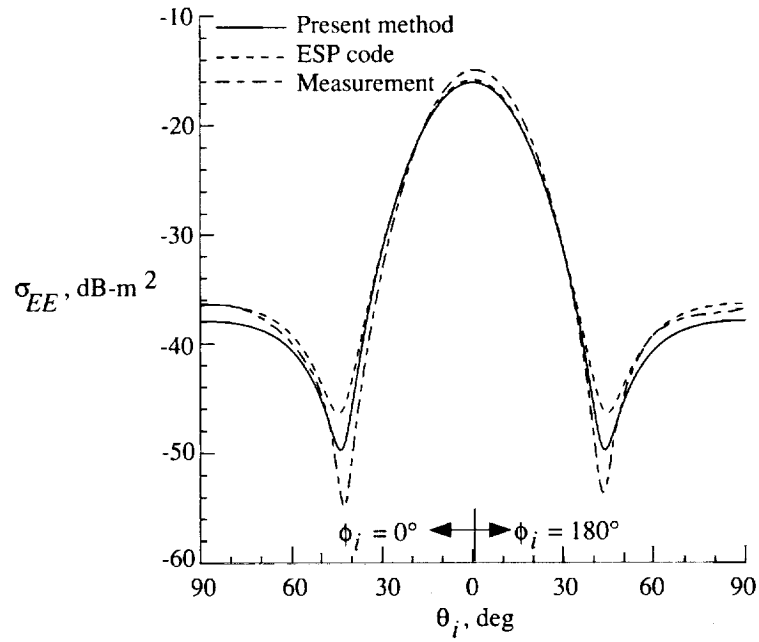


(b)  $E$ -polarized plane wave ( $\alpha_0 = 90^\circ$ ) at  $\phi_i = -90^\circ$  and  $90^\circ$ .

Figure 22. Monostatic RCS of diamond-shaped plate (shown in fig. 21) excited by  $H$ - and  $E$ -polarized plane waves ( $\alpha_0 = 0^\circ$  and  $90^\circ$ , respectively) as a function of  $\theta_i$  for  $f = 11.811$  GHz with  $M = N = 19$ .



(c)  $H$ -polarized plane wave ( $\alpha_0 = 0^\circ$ ) at  $\phi_i = 0^\circ$  and  $180^\circ$ .



(d)  $E$ -polarized plane wave ( $\alpha_0 = 90^\circ$ ) at  $\phi_i = 0^\circ$  and  $180^\circ$ .

Figure 22. Concluded.

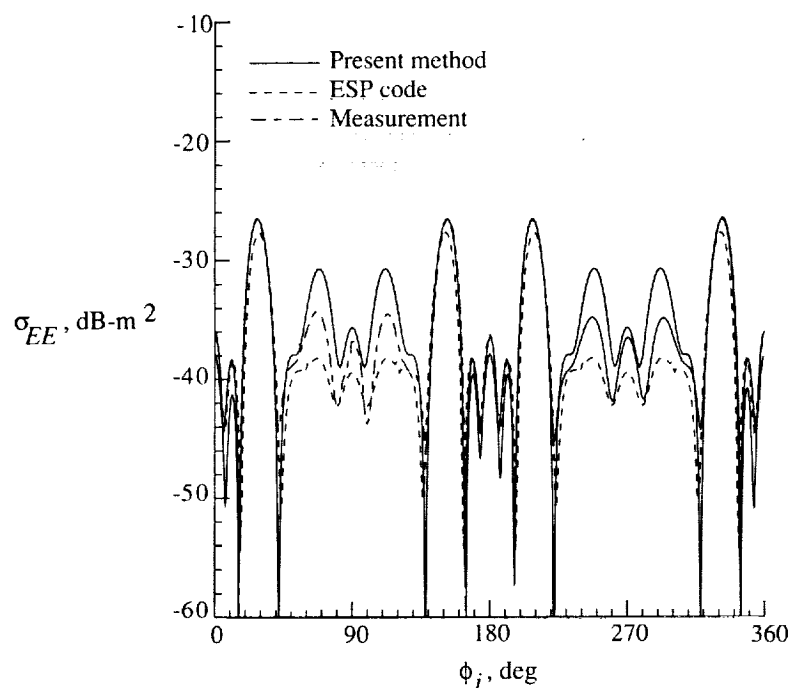


Figure 23. Monostatic RCS of diamond-shaped plate (shown in fig. 21) excited by  $E$ -polarized plane wave ( $\alpha_0 = 90^\circ$ ) as a function of  $\phi_i$  for  $f = 11.811$  GHz with  $M = N = 19$  and  $\theta_i = 90^\circ$  (grazing incidence).

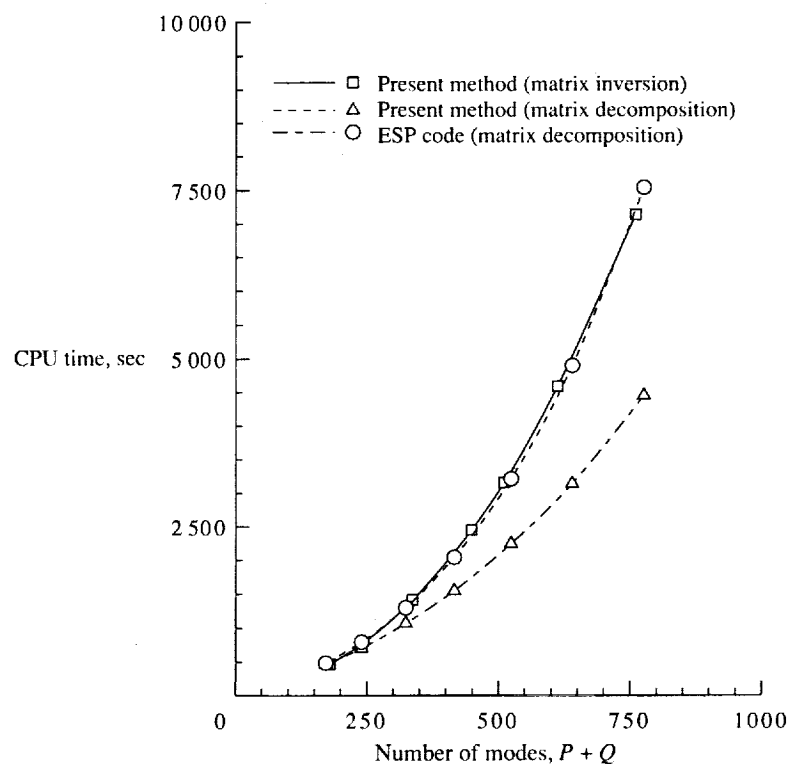


Figure 24. Comparison of CPU time required by present method using matrix inversion and decomposition with CPU time required by ESP code.



REPORT DOCUMENTATION PAGE			Form Approved OMB No. 0704-0188	
Public reporting burden for this collection of information is estimated to average 1 hour per response, including the time for reviewing instructions, searching existing data sources, gathering and maintaining the data needed, and completing and reviewing the collection of information. Send comments regarding this burden estimate or any other aspect of this collection of information, including suggestions for reducing this burden, to Washington Headquarters Services, Directorate for Information Operations and Reports, 1215 Jefferson Davis Highway, Suite 1204, Arlington, VA 22202-4302, and to the Office of Management and Budget, Paperwork Reduction Project (0704-0188), Washington, DC 20503.				
1. AGENCY USE ONLY (Leave blank)	2. REPORT DATE October 1993	3. REPORT TYPE AND DATES COVERED Technical Paper		
4. TITLE AND SUBTITLE Analysis of Electromagnetic Scattering From Irregularly Shaped, Thin, Metallic Flat Plates		5. FUNDING NUMBERS WU 505-64-70-01		
6. AUTHOR(S) Manohar D. Deshpande, C. R. Cockrell, Fred B. Beck, Erik Vedeler, and Melissa B. Koch				
7. PERFORMING ORGANIZATION NAME(S) AND ADDRESS(ES) NASA Langley Research Center Hampton, VA 23681-0001		8. PERFORMING ORGANIZATION REPORT NUMBER L-17218		
9. SPONSORING/MONITORING AGENCY NAME(S) AND ADDRESS(ES) National Aeronautics and Space Administration Washington, DC 20546-0001		10. SPONSORING/MONITORING AGENCY REPORT NUMBER NASA TP-3361		
11. SUPPLEMENTARY NOTES Deshpande: ViGYAN, Inc., Hampton, VA; Cockrell, Beck, Vedeler, and Koch: Langley Research Center, Hampton, VA.				
12a. DISTRIBUTION/AVAILABILITY STATEMENT  Unclassified Unlimited  Subject Category 32		12b. DISTRIBUTION CODE		
13. ABSTRACT (Maximum 200 words) This report describes an application of the method of moments to calculate the electromagnetic scattering from irregularly shaped, thin, metallic flat plates in free space. In the present technique, an irregularly shaped plate is enclosed by a rectangle on which the surface-current density is then expressed in terms of subdomain functions by dividing the rectangle into subsections. A shape function is introduced to ensure zero current outside the patch. The surface-current density is determined using the electric field integral equation (EFIE) approach in conjunction with the method of moments, and from a knowledge of the surface-current density, the electromagnetic scattering from a plate is calculated. Using this technique, the electromagnetic scattering from (1) a hexagonal plate, (2) an equilateral triangular plate, (3) an equilateral triangular plate with a concentric, equilateral triangular hole and an inverted, equilateral triangular hole, and (4) a diamond-shaped plate is computed and compared with the numerical results obtained by using the Electromagnetic Surface Patch (ESP) code developed by Ohio State University. The numerical results compare favorably with the measurements performed on these shapes in the Langley Experimental Test Range facility.				
14. SUBJECT TERMS Electromagnetic scattering; Moment method; Polygonal plates		15. NUMBER OF PAGES 49		
		16. PRICE CODE A03		
17. SECURITY CLASSIFICATION OF REPORT Unclassified	18. SECURITY CLASSIFICATION OF THIS PAGE Unclassified	19. SECURITY CLASSIFICATION OF ABSTRACT	20. LIMITATION OF ABSTRACT	